

An adaptable refinement approach for shell finite element models based on node-dependent kinematics

Original

An adaptable refinement approach for shell finite element models based on node-dependent kinematics / Li, G.; Carrera, E.; Cinefra, M.; de Miguel, A. G.; Pagani, A.; Zappino, E.. - In: COMPOSITE STRUCTURES. - ISSN 0263-8223. - 210:(2019), pp. 1-19. [10.1016/j.compstruct.2018.10.111]

Availability:

This version is available at: 11583/2722026 since: 2019-01-07T12:02:06Z

Publisher:

Elsevier

Published

DOI:10.1016/j.compstruct.2018.10.111

Terms of use:

This article is made available under terms and conditions as specified in the corresponding bibliographic description in the repository

Publisher copyright

Elsevier postprint/Author's Accepted Manuscript

© 2019. This manuscript version is made available under the CC-BY-NC-ND 4.0 license
<http://creativecommons.org/licenses/by-nc-nd/4.0/>. The final authenticated version is available online at:
<http://dx.doi.org/10.1016/j.compstruct.2018.10.111>

(Article begins on next page)

An Adaptable Refinement Approach for Shell Finite Element Models Based on Node-Dependent Kinematics

G. Li¹, E. Carrera^{1,2}, M. Cinefra¹, A. G. de Miguel¹, A. Pagani¹, E. Zappino^{1,*}

¹*MUL² Group, Department of Mechanical and Aerospace Engineering, Politecnico di Torino
Corso Duca degli Abruzzi 24, 10129 Torino, Italy.*

²*Laboratory of Intelligent Materials and Structures, Tambov State Technical University
Sovetskaya, 106, Tambov 392000, Russia*

Abstract

Towards improving the numerical efficiency in the analysis of multi-layered shell structures with the finite element (FE) method, an adaptable two-level mathematical refinement approach is proposed for refined curvilinear shell elements. Based on Carrera Unified Formulation (CUF), the approximation of displacement functions of shell elements can be improved by refining the through-the-thickness assumptions and enriching the shape functions. By using the hierarchical Legendre polynomial expansions (HLE) as shape functions, the element capabilities can be enhanced conveniently without re-meshing. To further increase the numerical efficiency of shell FE models, Node-Dependent Kinematics (NDK) is utilized to implement local kinematic refinements on the selected FE nodes within the domain of interest. The conjunction of NDK with the two-level refinements of the shell FE models leads to an adaptable refinement approach in the analysis of shell structures, which can be used to build FE models with optimal efficiency and high fidelity. The competence of the proposed approach is investigated through numerical studies on laminated shells.

Keywords: shell models, Carrera Unified Formulation, node-dependent kinematics, hierarchical Legendre polynomials

*Corresponding author. Tel: +39 011 090 6887, Fax: +39 011 090 6899.
Email address: enrico.zappino@polito.it (E. Zappino¹.)

1. Introduction

Thin-walled structures with curvatures, better known as shells, are vastly used in modern engineering. Shells span over large areas and can hold applied loads effectively, therefore are ideal to act as light-weight structures. A series of shell theories have been suggested, some of which have been widely adopted in structural analyzes. Traditional models include the classical theory based on KirchhoffLove assumption [1], the First-Order Shear Deformation Theory (FSDT) [2] built on the MindlinReissner assumption, and a variety of Higher-Order Theories [3, 4, 5]. Carrera [6] suggested a unified formulation (CUF) as a general framework to formulate continuum-based degenerated 2D models. CUF directly deals with the general terms of the approximation theories and leads to compact expressions of the governing equations in a unified form. Both of the two major types of models for laminated structures, namely the Equivalent Single-Layer (ESL) model, and the Layer-wise (LW) model, can be addressed in the framework of CUF.

Based on CUF, refined finite element (FE) models can be conveniently constructed through the *fundamental nuclei* (FNs) , a core unit of the structural stiffness matrix whose form is independent of the kinematics assumptions [7]. The adopted kinematic theories can be treated as the input parameters to the FE analyzes, leading to a variety of models with variable kinematics, in which the order of approximation expansions can be increased until the desired accuracy is achieved [8, 9]. Also, various and miscellaneous approximation theories can be employed to construct plate/shell FE models with high efficiency. Apart from commonly used Taylor series and Lagrange polynomials, the adoption of trigonometric, exponential, and hyperbolic series, as well as Legendre and Chebyshev polynomials, has also been discussed [10, 11]. A best-theory diagram was suggested to choose the most suitable theory for specific structural analyzes [12, 13, 14]. This variable kinematic approach has been extended to multi-field problems [15, 16, 17].

Node-Dependent Kinematics (NDK) is an FE approach proposed recently

in the framework of CUF [18, 19, 20]. By relating the kinematic assumptions to the chosen nodes, FE models with variable nodal kinematics can be built conveniently. NDK can be applied in the construction of FE models for concurrent global-local analysis. Naturally, the critical zone with higher-order assumptions
35 can be bridged to the less-critical area modeled with adequate lower-order theories [21]. ESL models and LW kinematics can coexist in the same element, making the FE model numerically optimal under the given accuracy requirements [22]. Besides, LW models can be used to model laminated structures with surface-mounted or embedded patches, such as piezo-electric components
40 [23]. In such cases, NDK can further make the numerical modeling procedure simplified by avoiding the use of 3D elements locally when accurate responses are needed [24, 25].

The p -version elements based on hierarchical polynomials were proposed in the 1970s [26, 27, 28]. Such elements are more efficient than the h -version refinement due to the fast convergence rate and can help to improve the numerical
45 accuracy on a given set of FE meshes. The avoidance of re-meshing is vital to shorten the overall simulation time consumption from the pre-processing phase. Meanwhile, their hierarchical characteristics make that the stiffness matrix of lower-order elements can be reused when an element with higher-order shape
50 functions is built [29, 30]. Recently, this type of functions defined on 2D domains were used as section functions of the refined beam models [31, 32] and were referred to as Hierarchical Legendre Expansions (HLE). Direct employment as shape functions on refined plate elements was reported by Zappino et al. [33]. Another advantage of the p -version 2D shape functions is that locking can be
55 sufficiently alleviated by increasing the polynomial order [29, 30, 34, 35, 36, 37]. Compared to the MITC technique (Mixed Interpolation of Tensorial Components [38, 39]), no additional shape functions are needed thus the extra loops in the FE routines and the corresponding time consumption is avoided. Interested readers can find a quantitative evaluation of shear and membrane locking in
60 hierarchical shell elements in the work by Li et al. [45].

In the framework of CUF, the refinement of the kinematic assumptions and

the increase of the order of the FE shape functions can be carried out at the same time with ease. This two-level refinement approach can lead to a broad spectrum of FE models on the given FE meshes. The combination of NDK
65 variable kinematics and p -version elements with HLE shape functions makes a powerful, adaptable approach for engineers to get improved numerical accuracy with controlled computational costs. In the authors' previous work [33], the HLE has been used in combination with NDK on plate element models. In this article, the construction of shell FE models through NDK and HLE is introduced, and
70 the modeling capabilities are examined through numerical assessments on shell structures.

2. Node-Dependent Kinematics shell FE formulation

2.1. Preliminaries

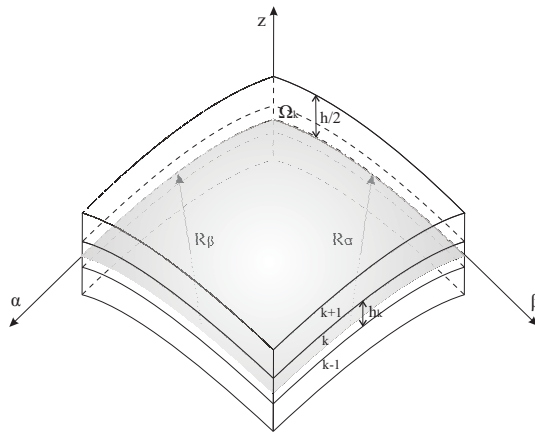


Figure 1: Notation of a shell model for laminated structures.

Shells are thin-walled structures with curvatures in geometry. As illustrated in Fig. 1, a typical shell structure can be described by using the curvilinear reference system (α, β, z) , in which α and β indicate the two “in-plane” directions and z the thickness direction. On a shell structure, the infinitesimal in-plane

area dS and the infinitesimal volume dV can be expressed as:

$$\begin{aligned} dS &= H_\alpha H_\beta d\alpha d\beta = H_\alpha H_\beta d\Omega, \\ dV &= H_\alpha H_\beta H_z d\alpha d\beta dz. \end{aligned} \quad (1)$$

in which $d\Omega$ is the infinitesimal in-plane area on the middle surface of the shell, and the coefficients H_α, H_β and H_z are:

$$H_\alpha = A(1 + z/R_\alpha), \quad H_\beta = B(1 + z/R_\beta), \quad H_z = 1. \quad (2)$$

In the above equation, R_α and R_β are the principal radii in the two in-plane directions of the middle surface, A and B the coefficients of the first fundamental form of Ω . For shells with constant curvatures (e.g., cylindrical and spherical shells), $A = B = 1$. In the present work, we consider only shells with constant curvatures. For more details about shell formulations, the reader is referred to [40, 41].

Defined in the curvilinear reference system as shown in Fig. 1, the strain and stress components can be arranged as:

$$\boldsymbol{\epsilon} = \{\epsilon_{\alpha\alpha}, \epsilon_{\beta\beta}, \epsilon_{zz}, \epsilon_{\alpha z}, \epsilon_{\beta z}, \epsilon_{\alpha\beta}\}^T \quad (3)$$

$$\boldsymbol{\sigma} = \{\sigma_{\alpha\alpha}, \sigma_{\beta\beta}, \sigma_{zz}, \sigma_{\alpha z}, \sigma_{\beta z}, \sigma_{\alpha\beta}\}^T \quad (4)$$

The strain vectors $\boldsymbol{\epsilon}$ can be obtained by means of the geometrical relations:

$$\boldsymbol{\epsilon} = \mathbf{b}\mathbf{u} \quad (5)$$

in which $\mathbf{u} = \{u, v, w\}^T$ is the displacement vector, and \mathbf{b} is the differential operators matrix, whose explicit expression reads:

$$\mathbf{b} = \begin{bmatrix} \frac{\partial_\alpha}{H_\alpha} & 0 & \frac{1}{H_\alpha R_\alpha} \\ 0 & \frac{\partial_\beta}{H_\beta} & \frac{1}{H_\beta R_\beta} \\ 0 & 0 & \partial_z \\ \partial_z - \frac{1}{H_\alpha R_\alpha} & 0 & \frac{\partial_\alpha}{H_\alpha} \\ 0 & \partial_z - \frac{1}{H_\beta R_\beta} & \frac{\partial_\beta}{H_\beta} \\ \frac{\partial_\beta}{H_\beta} & \frac{\partial_\alpha}{H_\alpha} & 0 \end{bmatrix} \quad (6)$$

The stress components can be attained from the constitutive equations as follows:

$$\boldsymbol{\sigma} = \tilde{\mathbf{C}}\boldsymbol{\epsilon} \quad (7)$$

in which $\tilde{\mathbf{C}}$ is the material coefficients matrix which is obtained by transforming its original form \mathbf{C} from the material coordinate system $(1, 2, 3)$ to the global system (α, β, z) . The original \mathbf{C} of a single orthotropic lamina in the material system reads:

$$\mathbf{C} = \begin{bmatrix} C_{11} & C_{12} & C_{13} & 0 & 0 & 0 \\ C_{21} & C_{22} & C_{23} & 0 & 0 & 0 \\ C_{31} & C_{32} & C_{33} & 0 & 0 & 0 \\ 0 & 0 & 0 & C_{44} & 0 & 0 \\ 0 & 0 & 0 & 0 & C_{55} & 0 \\ 0 & 0 & 0 & 0 & 0 & C_{66} \end{bmatrix} \quad (8)$$

80 The orthotropic material coefficients are characterized by nine independent coefficients, namely the Young's moduli, the shear moduli, and the Poisson ratios [4].

2.2. Carrera Unified Formulation (CUF) for refined shell models

According to Carrera Unified Formulation (CUF), the displacement field of a shell structure can be assumed to be:

$$\mathbf{u}(\alpha, \beta, z) = F_\tau(z)\mathbf{u}_\tau(\alpha, \beta) \quad (9)$$

in which $\mathbf{u}_\tau(\alpha, \beta)$ is the in-plane displacement vector, and $F_\tau(z)$ are related to 85 the theories of shell structures. The repeated index τ implies the application of Einstein's summation convention. The separation of variables provides the convenience to build a variety of bi-dimensional models for shell structures as elaborated in [7, 9, 10]. When higher-order polynomials are introduced to the definition of F_τ , refined shell theories are formulated, and better solution accuracy is expected to be obtained. The highest order of $F_\tau(z)$ can be increased 90 gradually until the solutions converge according to the chosen threshold.

Since $F_\tau(z)$ depends only on the thickness coordinates, they are also known as the thickness functions. When generating ESL models, $F_\tau(z)$ is expressed on the whole through-the-thickness domain of the multi-layered shells ($z \in [-\frac{h}{2}, \frac{h}{2}]$, h being the shell thickness), as illustrated in Fig. 2(a). Alternatively, for LW models, the displacements can be written as:

$$\mathbf{u}^k(\alpha, \beta, \zeta_k) = F_\tau^k(\zeta_k) \mathbf{u}_\tau^k(\alpha, \beta) \quad (10)$$

where $-1 \leq \zeta_k \leq 1$ is the adimensional thickness coordinate within layer k , as shown in Fig. 2(b). The displacement continuity conditions should be enforced at the layer interfaces in this case.

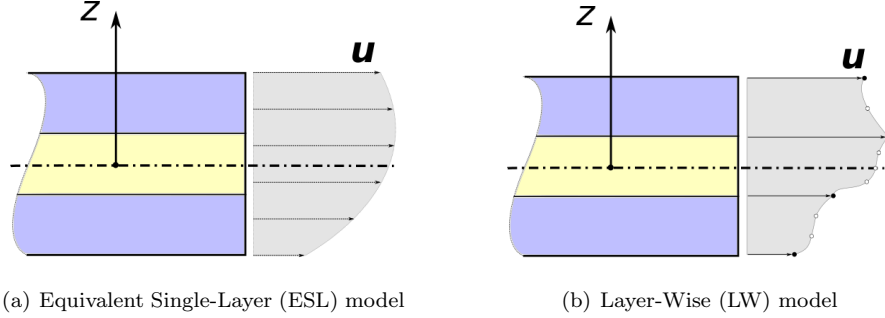


Figure 2: Two frameworks of models for multi-layered structures.

95 2.2.1. ESL models based on Taylor expansions (TE)

Taylor series $F_\tau = z^\tau$ can be adopted as thickness functions to build a set of ESL models. In numerical analyzes, if the highest order of the Taylor series is N , then there will be $N + 1$ terms, which read:

$$F_0 = z^0 = 1, \quad F_1 = z^1, \quad \dots, \quad F_N = z^N \quad (11)$$

Such a 2D model can be denoted as TE_N . FSDT [2] can be treated as a particular case of the complete linear model TE_1 . TE theories are the most commonly used in structural analyzes due to their inherent simplicity. Most times, they are adequate to get global structural responses such as displacements. While, when applied to heterogeneous structures such as laminated shells, TE theories
100 can not guarantee the continuity of the transverse stresses at layer interfaces.

2.2.2. LW models adopting Lagrange expansions (LE)

If F_τ^k are defined as Lagrange interpolation polynomials through the thickness of layer k , as expressed in Eq. 12, an LW model with LE kinematics can be built:

$$F_\tau^k(\zeta_k) = \prod_{i=0, i \neq s}^N \frac{\zeta_k - \zeta_{k_i}}{\zeta_{k_\tau} - \zeta_{k_i}} \quad (12)$$

where ζ_{k_τ} are located at the prescribed interpolation points, which are usually equally spaced through the thickness domain. $\zeta_{k_0} = -1$ and $\zeta_{k_N} = 1$ in the natural reference system represent the bottom and top surfaces of the k th layer, respectively.

To enforce the displacement continuity at the interfaces of two neighboring layers, the following constraint should be introduced:

$$u_t^k = u_b^{k+1}, \quad k = 1, \dots, N_l - 1. \quad (13)$$

in which N_l is the total number of layers, and the superscripts t and b stand for the top and bottom surfaces of their corresponding layer. The interfacial continuity of transverse stresses are not guaranteed but can be approximately achieved when enough LE terms are used in each layer as discussed by Carrera et al. [10].

2.3. Node-Dependent Kinematics (NDK)

Shape functions $N_i(\alpha, \beta)$ will be introduced to approximate displacement functions through the following expression when 2D models are discretized into FEs:

$$\mathbf{u}_\tau(\alpha, \beta) = N_i(\alpha, \beta) \mathbf{u}_{i\tau} \quad (14)$$

thus one obtains:

$$\mathbf{u}(\alpha, \beta, z) = N_i(\alpha, \beta) F_\tau(z) \mathbf{u}_{i\tau} \quad (15)$$

where $\mathbf{u}_{i\tau}$ are the unknowns to be calculated. In Eq. 15, the shape functions N_i and the thickness functions F_τ are independent. Carrera et al. [18, 19,

20] introduced a coupling by relating the thickness functions F_τ to the shape functions N_i through:

$$\mathbf{u}(\alpha, \beta, z) = N_i(\alpha, \beta) F_\tau^i(z) \mathbf{u}_{i\tau} \quad (16)$$

The difference of Eq. 16 from Eq. 15 is the additional superscript i of N_i , which is the index of the “anchoring” node of F_τ . This definition introduces the dependency of the kinematic assumptions on the FE nodes, namely the Node-Dependent Kinematics (NDK). According to NDK, the displacement field can be approximated through Eq. 17 for ESL models, in which $z \in [-\frac{h}{2}, \frac{h}{2}]$:

$$\begin{aligned} \mathbf{u}(\alpha, \beta, z) &= N_i(\alpha, \beta) F_\tau^i(z) \mathbf{u}_{i\tau} & \tau = 1, \dots, n_i; & \quad i = 1, \dots, m. \\ \delta \mathbf{u}(\alpha, \beta, z) &= N_j(\alpha, \beta) F_s^j(z) \delta \mathbf{u}_{js} & s = 1, \dots, n_j; & \quad j = 1, \dots, m. \end{aligned} \quad (17)$$

where n_i and n_j are the number of expansions on node i and j , respectively. m is the number of shape functions in the element. The displacement functions of LW models are written in Eq. 18, where $\zeta_k \in [-1, 1]$:

$$\begin{aligned} \mathbf{u}^k(\alpha, \beta, \zeta_k) &= N_i(\alpha, \beta) F_\tau^{ik}(\zeta_k) \mathbf{u}_{i\tau}^k & \tau = 1, \dots, n_i^k; & \quad i = 1, \dots, m. \\ \delta \mathbf{u}^k(\alpha, \beta, \zeta_k) &= N_j(\alpha, \beta) F_s^{jk}(\zeta_k) \delta \mathbf{u}_{js}^k & s = 1, \dots, n_j^k; & \quad j = 1, \dots, m. \end{aligned} \quad (18)$$

in which n_i^k and n_j^k are the number of adopted LW-type expansions in layer k on the corresponding nodes i and j , respectively. Note that the NDK technique
115 also allows for the dependency of the kinematic models on the layer, which can be useful when special attention should be paid to specific layers.

As mentioned before, thickness functions with an increased order provide the chance to the better approximation of the structure responses. With NDK, the kinematic models can be refined locally on specific nodes which makes it
120 easy to perform a local adaptable kinematic refinement. Different theories of structures will be blended naturally by the nodal shape functions within the element in-plane domain without any special coupling approaches. Meanwhile, no compatibility requirements for different nodal kinematics are needed. In the example shown in Fig. 3, the Q4 (four-node quadrilateral Lagrangian) element
125 owns four different theories on its four nodes.

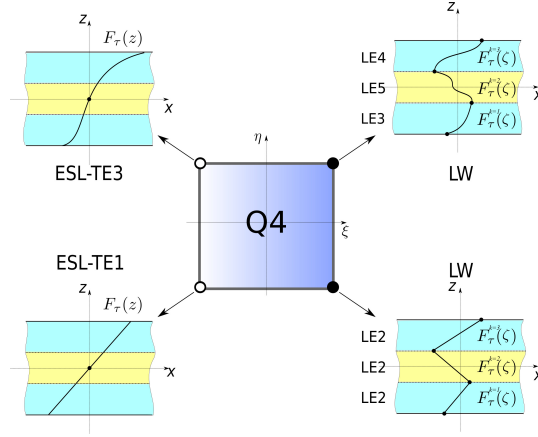


Figure 3: A Q4 element with different nodal kinematics.

The NDK technique can be applied to the efficient global-local modeling of structures. The kinematic model in the critical zone can be refined until the ideal accuracy is achieved while leaving the outlying region modeled with adequate lower-order theories. Global-local FE model can be constructed conveniently without modifying the meshes, and the same set of mesh grids can be re-used to build a family of models for concurrent global-local analyzes. This approach has been used in the efficient modeling of laminated structures in both 1D [18, 20] and 2D [19, 21, 22, 25] cases.

2.4. Hierarchical Legendre Expansions (HLE) as shape functions of 2D elements

A set of shape functions based on Legendre polynomials for a quadrilateral domain $(\xi, \eta) \in [-1, 1]$ was suggested by Szabó et al. [29, 30]. This type of shape functions can be classified into *nodal modes*, *edge modes*, and *internal modes*, as illustrated in Fig. 4.

Nodal modes are defined as Lagrange linear interpolation polynomials on the four vertex nodes of the quadrilateral domain, whose expressions are:

$$N_i(\xi, \eta) = \frac{1}{4}(1 - \xi_i\xi)(1 - \eta_i\eta) \quad i = 1, 2, 3, 4 \quad (19)$$

in which (ξ_i, η_i) represent the local coordinates of node i in the isoparametric reference system of a quadrilateral element.

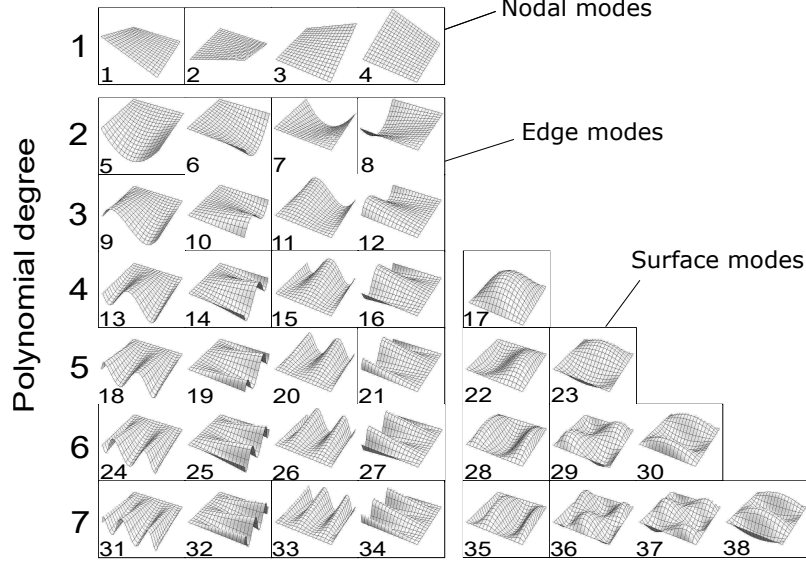


Figure 4: Higher-order Legendre polynomials as shape functions of 2D elements [30].

Edge modes are dominated by the deformation of the four edges and vanish linearly along the perpendicular edges. These functions are expressed as:

$$\begin{aligned}
 N_i(\xi, \eta) &= \frac{1}{2}(1 - \eta)\phi_p(\xi) & i = 5, 9, 13, 18, \dots \\
 N_i(\xi, \eta) &= \frac{1}{2}(1 + \xi)\phi_p(\eta) & i = 6, 10, 14, 19, \dots \\
 N_i(\xi, \eta) &= \frac{1}{2}(1 + \eta)\phi_p(\xi) & i = 7, 11, 15, 20, \dots \\
 N_i(\xi, \eta) &= \frac{1}{2}(1 - \xi)\phi_p(\eta) & i = 8, 12, 16, 21, \dots
 \end{aligned} \tag{20}$$

where ϕ_p is defined as:

$$\phi_p(\xi) = \sqrt{\frac{2p-1}{2}} \int_{-1}^{\xi} L_{p-1}(x) dx = \frac{L_p(\xi) - L_{p-2}(\xi)}{\sqrt{4p-2}} \quad p = 2, 3, \dots \tag{21}$$

Surface modes contain the deformation shapes that happen on the internal surface and vanish on the edges:

$$N_i(\xi, \eta) = \phi_m(\xi)\phi_n(\eta) \quad m, n \geq 2; \quad i = 17, 22, 23, 28, 29, 30, \dots \tag{22}$$

With the above hierarchical shape functions, four-node Legendre-type higher-order 2D elements can be formulated. Different from Lagrangian shape functions, when the polynomial degree p increases to $p + 1$, only the newly added

shape functions and the resulting matrices need to be introduced. Notably,
 145 compared with Lagrangian elements of the same polynomial order with equally
 spaced internal nodes, a fewer number of shape functions are needed. The
 polynomial order p can be treated as an input parameter, and mathematical
 enrichment can be conveniently realized on the same meshes to improve the
 numerical accuracy.

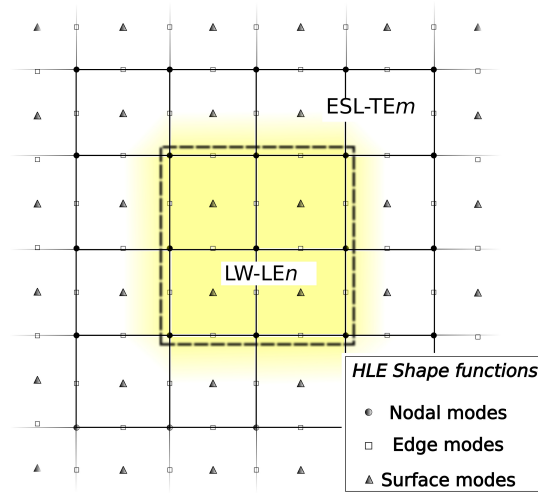


Figure 5: Assignment of nodal kinematics in 2D elements with HLE as shape functions.

150 For Lagrangian shape functions, each term corresponds to a specific node.
 While, for HLE shape functions, not every function has a specific position.
 When NDK is used on HLE-type elements, the “nodes” refer to the indexes
 of the shape functions directly. Each HLE function can have its individual
 kinematic model, but for simplicity purposes, in the present work, HLE shape
 155 functions of the same mode on the same edge or surface will be assigned to the
 same kinematic definition, as exhibited in Fig. 5. Determined by the definition
 of the shape functions, in HLE 2D elements, the “nodal” kinematics will be
 blended differently from the Lagrangian elements.

2.5. Governing equations of Node-Dependent Kinematic shell FE models

In FE applications, the governing equations of the shell FE models with NDK can be derived from the Principle of Virtual Displacements. For an elastic body in static equilibrium:

$$\delta L_{int} = \delta L_{ext} \quad (23)$$

where δL_{int} is the strain energy, and δL_{ext} the work done by the external loads on the virtual displacements. The internal work can be written as:

$$\delta L_{int} = \int_V \delta \boldsymbol{\epsilon}^T \boldsymbol{\sigma} dV = \int_{\Omega} \int_{A_k} \delta \boldsymbol{\epsilon}^T \boldsymbol{\sigma} H_{\alpha} H_{\beta} dz d\Omega \quad (24)$$

160 in which Ω represents the in-plane domain on the middle surface of the shell, and A_k the thickness domain of layer k .

By considering Eq. 17 or Eq.18 and Eq. 5, the strains can be obtained through the following expression which applies to both ESL and LW models:

$$\begin{aligned} \boldsymbol{\epsilon} &= \mathbf{b}N_i F_{\tau}^{i(k)} \mathbf{u}_{i\tau}^{(k)} \\ \delta \boldsymbol{\epsilon} &= \mathbf{b}N_j F_s^{j(k)} \mathbf{u}_{js}^{(k)} \end{aligned} \quad (25)$$

By substituting the strain expression in Eq. 25 and the constitutive relations in Eq. 7 into Eq. 24, one can get the internal work as:

$$\delta L_{int} = \delta \mathbf{u}_{js}^{(k)T} \mathbf{K}_{ij\tau s}^k \mathbf{u}_{i\tau}^{(k)} \quad (26)$$

where $\mathbf{K}_{ij\tau s}^k$ reads:

$$\mathbf{K}_{ij\tau s}^k = \int_{\Omega} \int_{A_k} (\mathbf{b}N_j F_s^{j(k)})^T \tilde{\mathbf{C}} (\mathbf{b}N_i F_{\tau}^{i(k)}) H_{\alpha} H_{\beta} dz d\Omega \quad (27)$$

This 3×3 matrix is the *fundamental nuclei* (FNs) of stiffness in the framework of CUF, the core unit of the element stiffness matrix. It contains nine nucleus components in the form of:

$$\mathbf{K}_{ij\tau s}^k = \begin{bmatrix} K_{\alpha\alpha} & K_{\alpha\beta} & K_{\alpha z} \\ K_{\beta\alpha} & K_{\beta\beta} & K_{\beta z} \\ K_{z\alpha} & K_{z\beta} & K_{zz} \end{bmatrix}_{ij\tau s}^k \quad (28)$$

The explicit expressions of the FNns are included in Appendix A.

Assume that $p_z(\alpha, \beta)$ is a distributed load acting on a spatial surface parallel to the middle surface of the shell, the virtual variation of the external work caused by p_z can be expressed as:

$$\delta L_{ext}^w = \int_{\Omega} \delta w(z_p) p_z H_{\alpha}(z_p) H_{\beta}(z_p) d\Omega = \delta w_{j_s}^{(k)} p_{j_s}^{z(k)} d\Omega \quad (29)$$

where z_p is the coordinate of the loading surface, and $p_{j_s}^{z(k)}$ reads:

$$p_{j_s}^{z(k)} = F_s^{j(k)}(z_p) H_{\alpha}(z_p) H_{\beta}(z_p) \int_{\Omega} N_j p_z d\Omega \quad (30)$$

By writing the surface load p_z into a vector as $\mathbf{p}_z(\alpha, \beta) = \{0, 0, p_z\}^T$, Eq. 29 can be further written into:

$$\delta L_{ext} = \delta \mathbf{u}_{j_s}^{(k)T} \mathbf{P}_{j_s}^{(k)} \quad (31)$$

where $\mathbf{P}_{j_s}^{(k)} = \{0, 0, p_{j_s}^{z(k)}\}^T$ are the FNs of the external load. Hence, the governing equations can be obtained as:

$$\delta \mathbf{u}_{j_s}^{(k)T} : \mathbf{K}_{ij\tau s}^k \mathbf{u}_{i\tau}^{(k)} = \mathbf{P}_{j_s}^{(k)} \quad (32)$$

By looping on the subscripts, the stiffness matrices and the load vector of the shell element can be built step by step. For more details about the assembly technique of FE models in the framework of CUF, see Carrera et al. [7]. In fact, it is straightforward to apply the standard CUF assembly routines to the NDK cases. The work of Zappino et al. [22] contains a discussion on this topic.

3. Numerical examples

Two benchmarks with analytical solutions are first studied for the verification of the proposed HLE shell elements adopting refined kinematics, including two-layered cylindrical shells and a group of spherical shells under distributed pressure. Then, three-layered spherical shells imposed to local bi-sinusoidal pressure are modeled and compared with the 3D FE solutions obtained with the commercial software ABAQUS. Besides the solution accuracy, the computational costs are also compared regarding the total number of degrees of freedom (DOFs) and the relative CPU time \bar{t} consumed in the solution.

In all the three numerical examples, LE kinematics is first used as thickness functions considering the high fidelity of LW models. In the numerical cases, LE kinematics of the same order will be applied to all the layers in a laminated shell. For comparison, TE kinematic theories (including FSDT) are tested. For the thick shells, FE models with Q9 (nine-node quadrilateral Lagrangian element) are assessed. For the thin shells, MITC9 (Q9 with MITC) elements are utilized to mitigate the locking phenomenon in the h -refinement approach when necessary. The related acronyms are included in Appendix B.

3.1. Two-layered cylindrical shells under distributed pressure

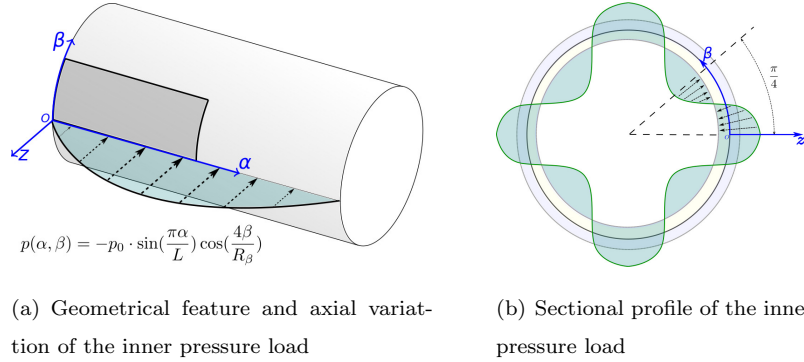


Figure 6: Geometry and loading of the two-layered cylindrical shells under distributed pressure.

This numerical case refers to the benchmark proposed by Varadan and Bhaskar [42]. The structures are cross-ply cylindrical shells with simple supports on both ends and subjected to transverse distributed pressure on the bottom surface. Fig. 6(a) presents the geometrical features of the structure, the axial variation of the pressure load, and the adopted reference system. Fig. 6(b) illustrates the sectional profile of the inner pressure. The distribution of the inner pressure follows:

$$p(\alpha, \beta) = -p_0 \sin \frac{\pi\alpha}{L} \cos \frac{4\beta}{R_\beta} \quad (33)$$

where L is the length of the shells and R_β the radius of the middle surface, and $L = 4R_\beta$. The circumference of the cylinder is $b = 2\pi R_\beta$, and the total

thickness is h . Three different radius-to-thickness ratios are considered, namely $R_\beta/h = 2, 100, \text{ and } 500$. The considered laminates consist of two plies of equal thickness with stacking sequence $(0^\circ/90^\circ)$ from bottom to top. The material coefficients of the lamina are taken to be: $E_L = 25E_T$, $G_{LT} = 0.5E_T$, $G_{TT} = 0.2E_T$, and $\nu_{LT} = \nu_{TT} = 0.25$, where L and T indicate the longitudinal and transverse direction of the fibers in the lamina, respectively. For comparison purposes, the results are non-dimensionalized through:

$$\begin{aligned} \bar{w} &= -\frac{10E_L h^3}{p_0 R_\beta^4}, & \bar{\sigma}_{\alpha\alpha} &= -\frac{10h^2}{p_0 R_\beta^2} \sigma_{\alpha\alpha}, & \bar{\sigma}_{\beta\beta} &= -\frac{10h^2}{p_0 R_\beta^2} \sigma_{\beta\beta}, & \bar{\sigma}_{\alpha\beta} &= -\frac{10h^2}{p_0 R_\beta^2} \sigma_{\alpha\beta}, \\ \bar{\sigma}_{\alpha z} &= -\frac{10h}{p_0 R_\beta} \sigma_{\alpha z}, & \bar{\sigma}_{\beta z} &= -\frac{10h}{p_0 R_\beta} \sigma_{\beta z}, & \bar{\sigma}_{zz} &= -\frac{1}{p_0} \sigma_{zz}. \end{aligned} \quad (34)$$

By making use of the cyclic/symmetric features, a 1/16 FE model can be built which covers 1/2 of the length and 1/8 of the circumference, as represented by the shaded area in Fig. 6(a). The FE models are first refined by increasing the order of thickness functions (F_t and F_s), then by raising the polynomial order of the shape functions (N_i, N_j). When only one element is used in the FE model, obviously HLE1 and HLE2 are not adequate and the p -refinement starts from HLE3 until HLE8. In the final step, the meshing is refined to explore the possibility of further improvement in accuracy.

The obtained results are summarized in Tables 1, 2, and 3. From the numerical results, it can be observed that the combination of refined kinematic shell models and higher order p -version 2D elements can give results with excellent agreement with the reference solutions. As shown in Fig. 7, when sufficiently refined LE models are used, through-the-thickness distribution of $\bar{\sigma}_{\alpha z}$, $\bar{\sigma}_{\beta z}$ are continuous at the interface of the two layers. Also, the variation of $\bar{\sigma}_{zz}$ shows that the shell models adopted are stretchable in the thickness direction. Comparatively, ESL models based on TE lead to good accuracy in the displacements and in-plane stresses but fail in the approximation of out-of-plane stresses. It can also be observed that for the thin shells ($R_\beta/h = 100$ and 500), with LE, a fewer number of expansions can lead to satisfactory results compared with the thick shell case ($R_\beta/h = 2$).

From Tables 2 and 3, it can be found that the transverse shear stresses $\bar{\sigma}_{\alpha z}$ and $\bar{\sigma}_{\beta z}$ obtained through Q9 elements are erroneous even if the meshes are quite refined. The results also manifest that adoption of MITC can effectively overcome this low convergence rate. For the HLE elements, the locking is mitigated by increasing the polynomial order gradually. This is especially obvious for the very thin shell ($R_\beta/h = 500$) whose results in Table 3 show that the HLE3 element is “locked” yet HLE8 is locking free. On the thin shells, the elements adopting higher-order Legendre-type shape functions with refined kinematics perform well and render themselves not sensitive to locking phenomena when the polynomial order is sufficiently high.

Table 1: Displacement and stress evaluation on the two-layered cylindrical shells, $R_\beta/h = 2$.

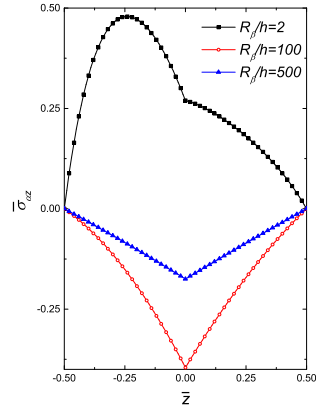
Theory(F_r, F_s)	FE(N_i, N_j)	Mesh	\bar{w} $(\frac{L}{2}, 0, 0)$	$\bar{\sigma}_{\alpha\alpha}$ $(\frac{L}{2}, 0, \frac{h}{2})$	$\bar{\sigma}_{\beta\beta}$ $(\frac{L}{2}, 0, \frac{h}{2})$	$\bar{\sigma}_{\alpha\beta}$ $(0, \frac{b}{16}, \frac{-h}{2})$	$\bar{\sigma}_{\alpha z}$ $(0, 0, \frac{-h}{4})$	$\bar{\sigma}_{\beta z}$ $(\frac{L}{2}, \frac{b}{16}, \frac{h}{4})$	$\bar{\sigma}_{zz}$ $(\frac{L}{2}, 0, \frac{h}{4})$	DOFs	
LE7	Q9	3×6	14.034	0.2517	9.564	-0.5139	0.5016	-3.006	-0.3156	4095	
		10×20	14.035	0.2515	9.756	-0.5026	0.4807	-2.938	-0.3132	38745	
TE1	HLE8	1×2	13.232	-0.02005	6.653	-0.3233	0.4321	-2.227	-0.4408	510	
TE3			13.590	0.2600	9.248	-0.4745	0.4294	-2.689	-0.3261	1020	
TE5			13.822	0.2637	9.615	-0.4961	0.4488	-2.832	-0.3129	1530	
LE3	HLE3	1×1	15.317	0.4371	8.563	-0.3941	0.3579	-3.131	-0.3359	252	
LE4			15.328	0.4085	8.597	-0.3950	0.3586	-3.133	-0.3372	324	
LE5			15.343	0.4293	8.685	-0.3954	0.3533	-3.028	-0.3293	396	
LE6			15.344	0.4236	8.678	-0.3954	0.3533	-3.028	-0.3291	468	
LE7			15.344	0.4257	8.681	-0.3954	0.3543	-3.037	-0.3300	540	
LE7			HLE4	14.002	0.3546	9.981	-0.5257	0.6039	-3.091	-0.2975	765
			HLE5	13.951	0.2609	10.09	-0.5077	0.4706	-2.989	-0.3056	1035
	HLE6	14.034	0.2494	9.762	-0.5029	0.4737	-2.945	-0.3127	1350		
	HLE7	14.036	0.2509	9.747	-0.5020	0.4788	-2.934	-0.3133	1710		
LE7	HLE8	1×2	14.035	0.2514	9.776	-0.5016	0.4786	-2.931	-0.3130	3825	
		2×4	14.035	0.2514	9.775	-0.5016	0.4786	-2.931	-0.3130	13005	
Varadan and Bhaskar [42]			14.034	0.2511	9.775	-0.5016	0.4786	-2.931	-0.31		

Table 2: Displacement and stress evaluation on the two-layered cylindrical shells, $R_\beta/h = 100$.

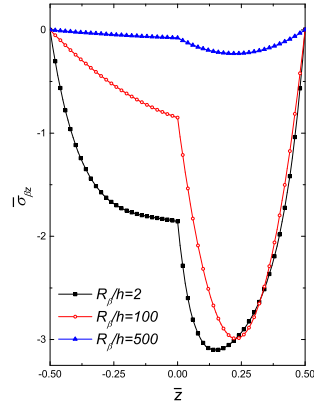
Theory(F_r, F_s)	FE(N_i, N_j)	Mesh	\bar{w} $(\frac{L}{2}, 0, 0)$	$\bar{\sigma}_{\alpha\alpha}$ $(\frac{L}{2}, 0, \frac{h}{2})$	$\bar{\sigma}_{\beta\beta}$ $(\frac{L}{2}, 0, \frac{h}{2})$	$\bar{\sigma}_{\alpha\beta}$ $(0, \frac{b}{16}, \frac{-h}{2})$	$\bar{\sigma}_{\alpha z}$ $(0, 0, \frac{-h}{4})$	$\bar{\sigma}_{\beta z}$ $(\frac{L}{2}, \frac{b}{16}, \frac{h}{4})$	$\bar{\sigma}_{zz}$ $(\frac{L}{2}, 0, \frac{h}{4})$	DOFs
LE3	Q9	6×12	1.359	0.1789	4.764	-0.3455	-0.04168	-7.897	-7.674	6825
		10×20	1.366	0.1844	5.282	-0.3457	-0.05320	-5.168	-7.956	18081
		15×30	1.367	0.1860	5.438	-0.3455	-0.07126	-4.003	-8.004	39711
LE3	MITC9	6×12	1.367	0.1882	5.592	-0.3491	-0.1516	-2.989	-7.749	6825
		10×20	1.367	0.1875	5.571	-0.3466	-0.1514	-2.979	-7.726	18081
		15×30	1.367	0.1873	5.565	-0.3459	-0.1513	-2.975	-7.717	39711
TE1	HLE8	2×4	1.356	0.2162	5.555	-0.3423	-0.2406	-1.889	50.53	1734
TE3			1.367	0.1868	5.559	-0.3452	-0.2448	-2.284	-6.769	3468
TE5			1.367	0.1867	5.560	-0.3452	-0.1387	-2.820	-5.887	5202
LE1	HLE3	1×1	0.1793	3.61E-03	-2.766	-0.02262	-2.635	5.587	1.990	108
LE2			0.1794	-1.31E-04	-2.772	-0.02262	-2.636	5.589	2.010	180
LE3			0.1794	5.43E-05	-2.772	-0.02262	-2.628	5.481	1.648	252
LE4			0.1794	5.15E-05	-2.772	-0.02262	-2.628	5.481	1.648	324
LE3	HLE4	1×1	1.062	0.2123	-8.10E-07	-1.27E-12	23.26	1.127	0.1536	357
	HLE5		1.301	0.2514	9.156	-0.2814	-8.026	-6.152	-8.960	483
	HLE6		1.361	0.1895	5.889	-0.3670	0.1842	-3.479	-7.704	630
	HLE7		1.366	0.1815	5.217	-0.3467	-0.05745	-2.988	-7.516	798
	HLE8		1.367	0.1867	5.537	-0.3453	-0.1610	-2.989	-7.708	987
LE3	HLE8	1×2	1.367	0.1872	5.561	-0.3452	-0.1527	-2.975	-7.709	1785
		2×4	1.367	0.1872	5.560	-0.3452	-0.1512	-2.972	-7.707	6069
		3×6	1.367	0.1872	5.560	-0.3452	-0.1512	-2.972	-7.707	12873
Varadan and Bhaskar [42]			1.367	0.1871	5.560	-0.3452	-0.1512	-2.972	-7.71	

Table 3: Displacement and stress evaluation on the two-layered cylindrical shells, $R_\beta/h = 500$.

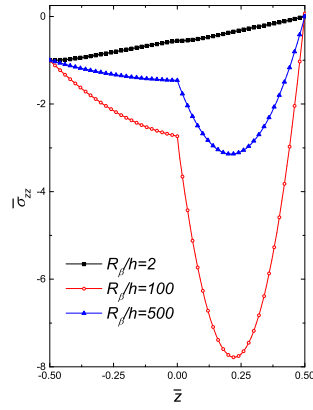
Theory(F_r, F_s)	FE(N_i, N_j)	Mesh	\bar{w} $(\frac{L}{2}, 0, 0)$	$\bar{\sigma}_{\alpha\alpha}$ $(\frac{L}{2}, 0, \frac{h}{2})$	$\bar{\sigma}_{\beta\beta}$ $(\frac{L}{2}, 0, \frac{h}{2})$	$\bar{\sigma}_{\alpha\beta}$ $(0, \frac{b}{16}, \frac{-h}{2})$	$\bar{\sigma}_{\alpha z}$ $(0, 0, \frac{-h}{4})$	$\bar{\sigma}_{\beta z}$ $(\frac{L}{2}, \frac{b}{16}, \frac{h}{4})$	$\bar{\sigma}_{zz}$ $(\frac{L}{2}, 0, \frac{h}{4})$	DOFs
LE3	Q9	10×20	0.1004	0.04390	0.3302	-0.1046	-0.07552	-1.184	-2.990	18081
		15×30	0.1005	0.04447	0.3883	-0.1046	-0.07552	-0.9957	-3.089	39711
LE3	MITC9	10×20	0.1005	0.04500	0.4354	-0.1049	-0.08424	-0.2279	-3.088	18081
		15×30	0.1005	0.04495	0.4349	-0.1047	-0.08417	-0.2276	-3.088	39711
TE1	HLE8	2×4	0.1005	0.04697	0.4367	-0.1044	-0.1216	-0.1482	74.80	1734
TE3			0.1005	0.04508	0.4347	-0.1045	-0.1206	-0.1792	-10.96	3468
TE5			0.1005	0.04477	0.4343	-0.1045	-0.07686	-0.2155	3.165	5202
LE1	HLE3	1×1	7.57E-03	-3.13E-03	-0.7363	-3.73E-03	-2.788	6.174	3.550	108
LE2			7.57E-03	-3.29E-03	-0.7365	-3.73E-03	-2.788	6.174	3.554	180
LE3			7.57E-03	-3.29E-03	-0.7365	-3.73E-03	-2.788	6.169	3.476	252
LE4			7.57E-03	-3.29E-03	-0.7365	-3.73E-03	-2.788	6.169	3.476	324
LE3	HLE4	1×1	0.0629	0.03145	-0.3267	-0.0478	34.49	4.057	18.07	357
	HLE5		0.0905	0.05295	1.353	-0.0789	-12.58	-6.901	-4.191	483
	HLE6		0.1005	0.04709	0.6831	-0.1121	0.32547	-0.8957	-4.138	630
	HLE7		0.1005	0.04424	0.3911	-0.1050	-0.02924	-0.0621	-3.182	798
	HLE8		0.1005	0.04490	0.4323	-0.1045	-0.08594	-0.2232	-3.091	987
LE3	HLE8	1×2	0.1005	0.04491	0.4346	-0.1045	-0.08923	-0.2261	-3.083	1785
		2×4	0.1005	0.04491	0.4345	-0.1045	-0.08410	-0.2274	-3.086	6069
		3×6	0.1005	0.04491	0.4345	-0.1045	-0.08410	-0.2274	-3.086	12873
Varadan and Bhaskar [42]			0.1005	0.0449	0.4345	-0.1045	-0.0841	-0.227	-3.09	



(a) $\bar{\sigma}_{\alpha z}$ through $(0, 0, \bar{z})$



(b) $\bar{\sigma}_{\beta z}$ through $(\frac{L}{2}, \frac{b}{16}, \bar{z})$



(c) $\bar{\sigma}_{zz}$ through $(\frac{L}{2}, 0, \bar{z})$

Figure 7: Through-the-thickness variation of transverse stresses on the two-layered cylindrical shells ($R_\beta/h = 2$: HLE8-LE7, Mesh=1×2; $R_\beta/h = 100$: HLE8-LE3, Mesh=2×4; $R_\beta/h = 500$: HLE8-LE3, Mesh=2×4).

3.2. Cross-ply spherical shells under sinusoidally distributed pressure

This section discusses the bending of cross-ply spherical shells, whose closed-form solutions were provided by Reddy [43]. The mechanical properties of each layer are assumed to be the same as the previous numerical case in Section. 3.1. The in-plane dimensions of the shell middle surface along the α and β axes are assumed to be $a/b = 1.0$, and the radii are considered being $R_\alpha = R_\beta = R$. The structure is subjected to bi-sinusoidally distributed load over the whole middle surface which reads:

$$p(\alpha, \beta) = p_0 \sin \frac{\pi\alpha}{a} \sin \frac{\pi\beta}{b} \quad (35)$$

The shells are simply supported on the four edges by following the boundary conditions as follows:

$$\begin{aligned} \alpha = 0, a : \quad & v = 0, w = 0; \\ \beta = 0, b : \quad & u = 0, w = 0. \end{aligned} \quad (36)$$

Various radius-to-thickness ratios (R/h) and side-to-thickness ratios (a/h) are considered. Laminates with stacking sequences ($0^\circ/90^\circ$) and ($0^\circ/90^\circ/90^\circ/0^\circ$) are analyzed. The results are reported regarding only the deflections at the central point $(\frac{a}{2}, \frac{b}{2}, 0)$ which are the reference results provided in [43]. The following non-dimensional parameters are used:

$$\bar{w} = \frac{h^3 E_T}{p_0 a^4} w \quad (37)$$

By making use of the symmetric boundary conditions, a 1/4 FE model is built. Table 4 summarizes the results for the two-layered shells with stacking sequence ($0^\circ/90^\circ$) including a thin shell ($a/h = 100$) and a moderate thick one ($a/h = 10$). The same refinement approach used in the last section is again adopted. Thickness functions are first refined, then the order of the HLE elements are gradually increased, while the mesh refinement is considered lastly. The best FE numerical solutions are obtained through LE kinematics and HLE shape functions. Table 5 reports results on the thin shells ($a/h = 100$) with lamination ($0^\circ/90^\circ/90^\circ/0^\circ$) with different radius-to-thickness ratios varying from 1 to 10^{30} . In fact, $R = a \times 10^{30}$ is equivalent to a plate case.

From Tables 4 and 5, it can be observed that the obtained results agree well
 235 with the closed-form solutions presented by Reddy [43]. The proposed conver-
 gence study procedure leads to models with greatly reduced DOFs compared
 with the h -refinement with MITC9 elements. It can be found that, if the re-
 sults are evaluated concerning only displacements (\bar{w}), lower-order models can
 be adequate most times, and higher-order kinematics of either ESL- or LW-
 240 type might not be necessary. More detailed comparison of different modeling
 approaches should be made regarding not only the displacements but also the
 stresses.

Table 4: Cross-ply spherical shells with ($0^\circ/90^\circ$) under bi-sinusoidally distributed pressure,
 $R/h = 5$.

$a/h = 100$					$a/h = 10$				
Theory(F_τ, F_s)	FE(N_i, N_j)	Mesh	\bar{w}	DOFs	Theory(F_τ, F_s)	FE(N_i, N_j)	Mesh	\bar{w}	DOFs
FSDT			1.1947	190	FSDT			11.181	190
TE1	HLE7	1×1	1.1958	228	TE1	HLE7	1×1	11.189	228
TE3			1.1949	456	TE7			11.406	912
TE5			1.1949	684	TE9			11.411	912
		1×1	1.2317	135			1×1	11.528	243
LE2	MITC9	2×2	1.1981	375	LE4	MITC9	2×2	11.435	675
		4×4	1.1951	1215			4×4	11.427	2187
		8×8	1.1949	4335			8×8	11.427	7803
LE1	HLE2	1×1	0.6374	72	LE1			9.975	72
LE2			0.6377	120	LE2	HLE2	1×1	10.063	120
LE2	HLE3		1.1054	180	LE3			10.141	168
LE2	HLE4		1.1788	180	LE4			10.141	216
LE2	HLE5	1×1	1.1930	345	LE4	HLE3		10.738	324
LE2	HLE6		1.1950	450	LE4	HLE4		11.334	459
LE2	HLE7		1.1949	570	LE4	HLE5	1×1	11.421	621
LE3	HLE7		1.1949	798	LE4	HLE6		11.428	810
LE2	HLE7	2×2	1.1949	1815	LE4	HLE7		11.427	1026
					LE5	HLE7		11.427	1254
					LE4	HLE7	2×2	11.427	3267
	Reddy[43]		1.1948			Reddy[43]		11.429	

Table 5: Cross-ply spherical shells with $(0^\circ/90^\circ/90^\circ/0^\circ)$ under bi-sinusoidally distributed pressure, $a/h = 100$.

R/a	Theory(F_τ, F_s)	FE(N_i, N_j)	Mesh	\bar{w}	DOFs
1	LE2	HLE7	1×1	0.05323	1026
	LE2	MITC9	8×8	0.05323	7803
	FSDT	HLE7	1×1	0.05322	190
	TE5	HLE7	1×1	0.05323	684
Reddy[43]				0.0532	
5	LE2	HLE7	1×1	1.0286	1026
	LE2	MITC9	8×8	1.0286	7803
	FSDT	HLE7	1×1	1.0277	190
	TE5	HLE7	1×1	1.0285	684
Reddy[43]				1.0279	
10^{30}	LE2	HLE7	1×1	4.3463	1026
	LE2	MITC9	4×4	4.3463	7803
	FSDT	HLE7	1×1	4.3327	190
	TE5	HLE7	1×1	4.3451	684
Reddy[43]				4.3368	

3.3. *Simply supported three-layered cross-ply spherical shells under local bi-sinusoidally distributed pressure*

This section reports numerical results of simply supported three-layered cross-ply spherical shells subjected to local bi-sinusoidally distributed pressure. The lamination sequence is $(90^\circ/0^\circ/90^\circ)$. The three layers have equal thickness $h/3$. The mechanical properties of each lamina are the same as in Section. 3.1. The geometrical features and loading are illustrated in Fig. 8. The origin point of the curvilinear reference system is placed at the central point of the spherical shells. The middle-surface radii are assumed to be $R_\alpha = R_\beta = R = 1$. The local pressure is subjected to the top surface, and its distribution follows:

$$p(\alpha, \beta) = -p_0 \cos \frac{\pi\alpha}{a/10} \cos \frac{\pi\beta}{b/5} \quad (38)$$

where a and b are dimensions of the spherical shells in α and β direction, respectively. $p_0 = 1$ is the magnitude of the pressure load. The loaded region covers the central area of $\frac{a}{10} \times \frac{b}{5}$. Simple supports are imposed on the four edges, which follow:

$$\begin{aligned} \alpha = \pm \frac{a}{2} : \quad v = 0, w = 0; \\ \beta = \pm \frac{b}{2} : \quad u = 0, w = 0. \end{aligned} \quad (39)$$

Radius-to-thickness ratios in a wide range ($R/h = 10, 100, 1000$) are studied. For the convenience of comparison, the deflection and stresses are reported by using the following dimensionless parameters:

$$\begin{aligned} \bar{w} = -\frac{10^6 E_L h^3}{p_0 R^4} w, \quad \bar{\sigma}_{\alpha\alpha} = -\frac{10^4 h^2}{p_0 R^2} \sigma_{\alpha\alpha}, \quad \bar{\sigma}_{\beta\beta} = -\frac{10^4 h^2}{p_0 R^2} \sigma_{\beta\beta}, \quad \bar{\sigma}_{zz} = -\frac{1}{p_0} \sigma_{zz}, \\ \bar{\sigma}_{\alpha z} = \frac{100h}{p_0 R} \sigma_{\alpha z}, \quad \bar{\sigma}_{\beta z} = \frac{100h}{p_0 R} \sigma_{\beta z}, \quad \bar{\sigma}_{\alpha\beta} = -\frac{10^5 h^2}{p_0 R^2} \sigma_{\alpha\beta}. \end{aligned} \quad (40)$$

245

By considering the symmetric boundary conditions, a quarter of the structure is modeled. The 1/4 FE model contains 10×10 elements, among which the local pressure load covers the in-plane range of two elements, as illustrated in Fig. 8. The FE models on the given meshes are mathematically enriched until

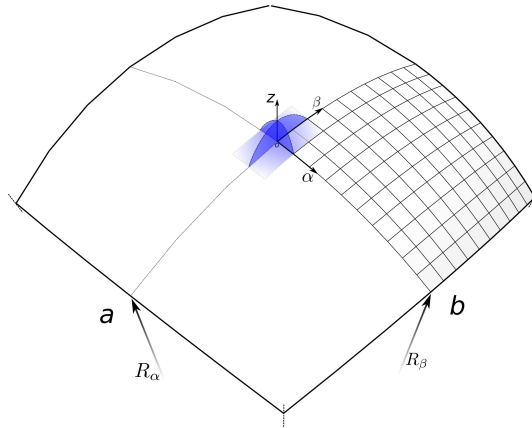


Figure 8: Three-layered cross-ply spherical shells subjected to local bi-sinusoidally distributed pressure.

250 numerical convergence is achieved with the threshold of 1%. Then, NDK approach is used to construct efficient FE models with local refinement to capture the regional effects caused by the pressure.

For the verification of the adopted refined FE shell models, C3D20R (20-node quadratic brick element with reduced integration) in the commercial software
 255 ABAQUS is used to build 3D FE models. It should be noted that for brick elements, the stresses at a node are extrapolated from the integration point values (exact values). Another issue is that the high aspect ratio (span-to-thickness ratio) should be avoided when brick elements are used. Generally, the aspect ratio should not exceed 10 to avoid the potential poor accuracy [44].
 260 Depending on the structural features and the boundary conditions as well as the loading, the high aspect ratios will not necessarily lead to inaccurate results. In the meantime, to obtain detailed stress field, at least five layers of hexahedral elements are used in each lamina in the present work. When the shell becomes thinner, more refined in-lane meshes are needed to reduce the aspect ratio. For the very thin shell with $R/h = 1000$, the effective 3D FE modeling will be very
 265 computationally expensive and was not considered. Table 6 summarizes the maximum aspect ratios of the brick elements used in the 3D FE models. It can

be found that in the thin shell with $R/h = 100$, one of the 3D models contains elements exceeding the aspect ratio of 10 which is not preferred.

Table 6: Maximum aspect-ratios of C3D20R brick elements in the 3D models for the three-layered spherical shells under local distributed pressure.

R/h	Mesh($\alpha \times \beta \times z$)	Element aspect ratio
10	$50 \times 50 \times 5$	1.7
	$50 \times 50 \times 10$	3.3
100	$50 \times 50 \times 5$	15.8
	$100 \times 100 \times 5$	7.9

270 The obtained results have been summarized in Tables 7, 8, and 9. The CPU time values \bar{t} listed are relative to the cheapest model (Mesh 10×10 , HLE2-LE1). Since the FSDT model is treated as a particular case of TE1 by using a penalty method in the in-house FE code used to collect the numerical results, its CPU time cannot reflect the actual efficiency thus is omitted. Also, for a
 275 fair comparison, the CPU time consumptions of ABAQUS 3D models are not listed.

From numerical results in Tables 7 and 8, and the comparison of the transverse shear stresses in Figs. 10 and 11, it can be observed that, when numerical convergence is achieved (through 10×10 elements, HLE5-LE5 for $R/h = 10$,
 280 and HLE6-LE4 for $R/h = 100$), great agreement with the C3D20R 3D models is reached, and the maximum relative error is less than 1% for the deflection and the stresses. In fact, 2D elements are free of the aspect ratio problem related to the thickness dimension of thin structures, and the use of CUF empowers the shell elements with adequately refined thickness functions to achieve 3D
 285 accuracy. From Tables 7, 8, and 9, it can be found that with the increase of the radius-to-thickness ratio R/h , lower-order LE thickness functions are already sufficient in reaching the convergence. Meanwhile, higher-order shape functions are required to obtain satisfactory results. Since these refinements are mathematical, the re-meshing work (h -version approach) can be reduced to the

Table 7: Deflection and stress evaluation on the three-layered spherical shells under local pressure, $R/h = 10$.

Mesh ($\alpha \times \beta$)	Theory (F_r, F_θ)	Element (N_i, N_j)	\bar{w} (0,0,0)	$\bar{\sigma}_{\alpha\alpha}$ (0, 0, $\frac{h}{6}$)	$\bar{\sigma}_{\beta\beta}$ (0, 0, $\frac{h}{2}$)	$\bar{\sigma}_{\alpha\beta}$ ($\frac{a}{20}, \frac{b}{10}, \frac{-h}{2}$)	$\bar{\sigma}_{\alpha z}$ ($\frac{a}{25}, 0, 0$)	$\bar{\sigma}_{\beta z}$ (0, $\frac{2b}{25}, 0$)	$\bar{\sigma}_{zz}$ (0, 0, $\frac{h}{2}$)	Total shape functions	DOFs	CPU time \bar{t}
10×10	LE1	HLE2	5607	265.9	425.8	101.2	3.037	1.702	0.8903	341	4092	1.0
	LE2		5669	311.6	512.7	112.4	3.005	1.637	1.088	341	7161	2.0
	LE3		5718	355.6	552.3	117.9	3.506	1.717	1.050	341	10230	3.5
	LE4		5718	356.1	552.4	118.1	3.506	1.716	1.029	341	13299	5.9
	LE5		5719	357.5	550.8	118.2	3.432	1.716	1.024	341	16368	8.6
	LE6		5719	357.4	550.5	118.2	3.433	1.716	1.024	341	19437	11.9
10×10		HLE3	5722	363.8	539.3	110.8	3.428	1.769	0.9889	561	26928	20.5
	LE5	HLE4	5726	361.8	537.4	110.8	3.435	1.771	1.000	881	42288	45.0
		HLE5	5727	361.4	537.5	111.2	3.426	1.770	1.001	1301	62448	88.9
10×10	FSDT		5320	365.5	252.7	92.18	2.940	1.104	–	1301	6505	–
	TE1	HLE5	5290	352.5	264.3	87.24	2.914	1.113	0.5265	1301	7806	3.8
	TE3		5590	274.4	499.9	109.3	3.220	1.512	1.100	1301	15612	14.1
	TE5		5623	257.8	521.8	108.2	3.046	1.577	1.003	1301	23418	31.8
10×10			5724	376.6	565.7	122.7	3.413	1.713	1.030	441	21168	66.3
20×20			5727	367.4	544.2	114.4	3.335	1.770	1.005	1681	80688	308.9
30×30	LE5	MITC9	5727	364.2	540.4	112.7	3.386	1.770	1.002	3721	178608	841.5
40×40			5727	363.0	539.2	112.1	3.426	1.766	1.001	6561	314928	5742.2
50×50			5727	362.4	538.6	111.8	3.453	1.774	1.001	10201	489648	9789.1
10×10	TE1/LE5 ^{×6}		5522	361.0	543.3	110.5	3.437	1.693	1.001	1301	11922	7.7
	TE1/LE5 ^{×12}		5603	360.9	545.7	111.7	3.418	1.739	1.001	1301	15366	11.7
	TE1/LE5 ^{×20}	HLE5	5655	361.4	545.0	111.5	3.421	1.758	1.001	1301	19818	17.4
	TE3/LE5 ^{×20}		5694	360.9	538.8	111.2	3.425	1.766	1.001	1301	25908	25.7
	TE5/LE5 ^{×20}		5713	361.2	538.2	111.2	3.426	1.770	1.001	1301	31998	41.6
50 × 50 × 5 [‡]		C3D20R*	5680	349.3	519.7	108.3	3.291	1.744	1.005	162231	486693	–
50 × 50 × 10 [‡]			5680	358.6	528.2	109.1	3.403	1.757	1.001	316761	950283	–

‡ Mesh ($\alpha \times \beta \times z$);

* ABAQUS 20-node quadratic brick element with reduced integration.

Table 8: Deflection and stress evaluation on the three-layered spherical shells under local pressure, $R/h = 100$.

Mesh ($\alpha \times \beta$)	Theory (F_r, F_s)	Element (N_i, N_j)	\bar{w} (0,0,0)	$\bar{\sigma}_{\alpha\alpha}$ (0, 0, $\frac{h}{6}$)	$\bar{\sigma}_{\beta\beta}$ (0, 0, $\frac{h}{2}$)	$\bar{\sigma}_{\alpha\beta}$ ($\frac{a}{20}, \frac{b}{10}, \frac{-h}{2}$)	$\bar{\sigma}_{\alpha z}$ ($\frac{a}{25}, 0, 0$)	$\bar{\sigma}_{\beta z}$ (0, $\frac{2b}{25}, 0$)	$\bar{\sigma}_{zz}$ (0, 0, $\frac{h}{2}$)	Total shape functions	DOFs	CPU time \bar{t}
10×10	LE1		185.6	91.53	104.1	52.05	2.145	1.941	2.088	341	4092	1.0
	LE2		186.2	91.61	104.4	52.39	2.154	1.939	1.277	341	7161	1.7
	LE3	HLE2	186.2	91.52	104.5	52.49	2.712	1.948	1.295	341	10230	3.1
	LE4		186.2	91.52	104.5	52.49	2.712	1.948	1.304	341	13299	4.8
	LE5		186.2	91.52	104.5	52.49	2.706	1.948	1.304	341	16368	7.0
10×10		HLE3	189.8	111.7	111.0	49.26	2.328	2.386	0.9956	561	21879	11.0
		HLE4	190.1	106.5	109.8	49.17	2.535	2.403	0.9891	881	34359	24.2
		HLE5	190.2	106.0	109.5	49.26	2.493	2.391	0.9994	1301	50739	48.3
		HLE6	190.2	106.2	109.6	49.32	2.483	2.388	1.000	1821	71019	89.2
10×10	FSDT		187.0	104.8	107.5	48.26	1.490	0.895	–	1821	9105	–
	TE1	HLE6	187.2	104.9	107.5	48.26	1.490	0.896	4.022	1821	10926	5.6
	TE3		189.1	105.2	109.6	49.06	1.989	1.727	1.151	1821	21852	20.0
	TE5		189.6	105.5	109.5	49.16	2.062	2.169	0.9900	1821	32778	45.7
10×10			190.0	116.2	114.4	54.20	2.502	2.284	1.123	441	17199	36.6
20×20			190.2	110.8	111.0	50.88	2.357	2.394	1.034	1681	65559	168.4
30×30	LE4	MITC9	190.2	108.4	110.2	50.08	2.426	2.391	1.009	3721	145119	477.4
40×40			190.2	107.5	109.9	49.76	2.488	2.381	1.003	6561	255879	3377.8
50×50			190.2	107.0	109.8	49.61	2.533	2.399	1.001	10201	397839	5875.8
10×10	TE1/LE4 ^{×6}		190.0	106.2	109.5	49.13	2.482	2.389	1.003	1821	15315	9.3
	TE1/LE4 ^{×12}	HLE6	190.1	106.2	109.5	49.26	2.482	2.389	1.000	1821	19077	13.2
	TE3/LE4 ^{×12}		190.2	106.2	109.6	49.31	2.483	2.388	1.000	1821	28521	27.0
50 × 50 × 5 [‡]		C3D20R*	192.4	106.7	110.5	49.48	2.463	2.394	0.9886	162231	486693	–
100 × 100 × 5 [‡]			192.1	106.4	110.1	49.30	2.459	2.389	1.000	639431	1918293	–

‡ Mesh ($\alpha \times \beta \times z$);

* ABAQUS 20-node quadratic brick element with reduced integration.

Table 9: Deflection and stress evaluation on the three-layered spherical shells under local pressure, $R/h = 1000$.

Mesh ($\alpha \times \beta$)	Theory (F_T, F_s)	Element (N_i, N_j)	\bar{w} (0,0,0)	$\bar{\sigma}_{\alpha\alpha}$ ($0, 0, \frac{h}{6}$)	$\bar{\sigma}_{\beta\beta}$ ($0, 0, \frac{h}{2}$)	$\bar{\sigma}_{\alpha\beta}$ ($\frac{a}{20}, \frac{b}{10}, \frac{-h}{2}$)	$\bar{\sigma}_{\alpha z}$ ($\frac{a}{25}, 0, 0$)	$\bar{\sigma}_{\beta z}$ ($0, \frac{2b}{25}, 0$)	$\bar{\sigma}_{zz}$ ($0, 0, \frac{h}{2}$)	Total shape functions	DOFs	CPU time \bar{t}
10×10		LE1	5.011	5.423	8.499	13.56	1.634	-0.9300	6.446	341	4092	1.0
		LE2	5.012	5.410	8.487	13.56	1.634	-0.9280	2.392	341	7161	1.6
		LE3	5.012	5.410	8.487	13.56	1.678	-0.9279	2.429	341	10230	3.1
		LE4	5.012	5.410	8.487	13.56	1.678	-0.9279	2.433	341	13299	4.7
10×10	LE3	HLE3	5.986	14.16	18.73	11.95	-0.0323	-0.1520	1.094	561	16830	7.3
		HLE4	6.160	15.68	19.01	13.31	-0.5414	0.2285	0.9472	881	26430	15.5
		HLE5	6.216	15.15	17.72	13.24	0.3871	0.5052	0.9819	1301	39030	29.9
		HLE6	6.219	15.12	17.72	13.25	0.3847	0.4946	1.036	1821	54630	72.3
		HLE7	6.219	15.10	17.77	13.25	0.3809	0.4829	1.000	2441	73230	93.1
		HLE8	6.219	15.09	17.76	13.25	0.3865	0.4852	1.000	3161	94830	142.1
10×10		FSDT	6.217	15.09	17.77	13.25	0.2336	0.1746	-	3161	15805	-
		TE1	6.227	15.19	17.80	13.25	0.2339	0.1748	36.05	3161	18966	13.9
		TE3	6.218	15.09	17.77	13.25	0.3092	0.3449	0.7835	3161	37932	54.1
		TE5	6.218	15.09	17.77	13.25	0.3206	0.4396	1.353	3161	56898	124.5
10×10			6.314	17.56	19.80	14.52	0.4110	0.4424	2.304	441	13230	23.7
20×20			6.227	15.86	18.16	13.65	0.3422	0.4920	1.509	1681	50430	128.2
30×30	LE3	MITC9	6.220	15.43	17.92	13.46	0.3633	0.4861	1.082	3721	111630	380.5
40×40			6.219	15.28	17.85	13.38	0.3903	0.4813	1.018	6561	196830	741.1
50×50			6.219	15.21	17.82	13.34	0.4137	0.4915	1.006	10201	306030	1245.9
10×10	TE1/LE3 ^{×6}	HLE8	6.219	15.09	17.76	13.25	0.3865	0.4852	1.004	3161	24270	19.4
	TE1/LE3 ^{×12}		6.219	15.09	17.76	13.25	0.3865	0.4852	1.000	3161	28974	24.6

290 minimum. Fig. 12 shows that the employed refined shell FE models are capable
of obtaining 3D stress fields in detail. For the convenience of observation, the
thickness dimensions of the thin shells in Fig. 12 are scaled by certain times.

Again, with TE kinematics, the deflection and in-plane stresses are accurate,
yet the transverse stresses are not always reliable. If only the global displacement
295 responses are required, TE kinematics are preferred to LE theories mainly due to
its relatively low computational costs. Compared to models with HLE elements
with equal accuracy, models with MITC9 elements will contain a lot more shape
functions and consume longer computational time. From the comparison, it can
also be observed that the adopted higher-order HLE elements are not sensitive
300 to locking even for the very thin shell with $R/h = 1000$.

The NDK technique can be employed to construct FE models with variable
TE/LE nodal kinematics, in which the refined LE kinematics is only assigned
to the nodes within and adjacent to the loaded region. In fact, shells with
different radius-to-thickness ratios (R/h) need different locally refined zones
305 to guarantee the accuracy. Fig. 9 compares three models with different local
regions, in which TE_m represents TE thickness functions of order m , and LE_n
stands for LE kinematics of order n . The superscripts of $LE_n^{\times N_e}$ indicate the
number of elements employing the refined theory LE_n on all of their subordinate
nodes, and their corresponding area has been indicated in Fig. 9. It should be
310 noted that the rest of the nodes in the FE models will adopt TE_m assumptions.

The obtained results in Table 7 show that the moderate-thick shell with
 $R/h = 10$ needs a comparatively large locally refined area, which is NDK model
C in Fig. 9(c) with HLE5-TE5/LE5 $^{\times 20}$. For the thin and very thin shells, the lo-
cally refined area consists of twelve p -version elements is already sufficient, which
315 correspond to NDK model B in Fig. 9(b). The refinement of the TE theories in
the non-critical zone also has a great contribution to the accurate approximation
of the stresses in the critical region, especially for the thick shell with $R/h = 10$.
From the results in Tables 7, 8, and 9, it can be concluded that, compared to
the uniformly refined FE models, the NDK models adopted can help reduce the
320 computational costs considerably without sacrificing the accuracy. A detailed

comparison of the through-the-thickness variation of transverse shear stresses in Fig. 10 and Fig. 11 also shows the great agreement of results obtained with the NDK models with the uniformly refined models. By comparing Fig. 13 with Fig. 12, it can also be found that the NDK models can reproduce the stress fields of those obtained with uniformly refined FE models with consistency. As shown in Table 10, compared with the uniform kinematic refinements, the NDK model is particularly efficient for the very thin shell ($R/h = 1000$) which leads to a reduction of 69.4% regarding the DOFs and a decrease of 82.7% in the solution time. Even for the thick shell ($R/h = 10$), the solution consumptions can be saved by around 50%.

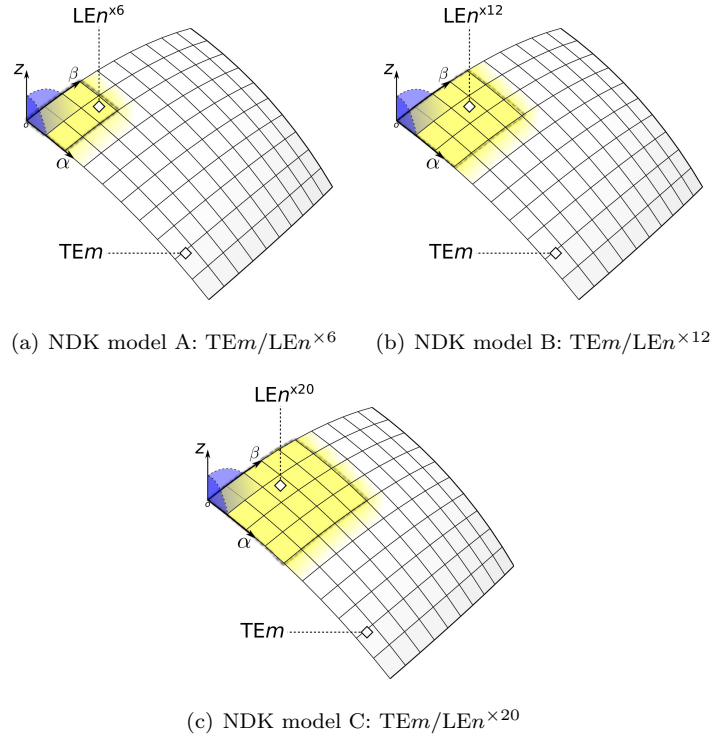
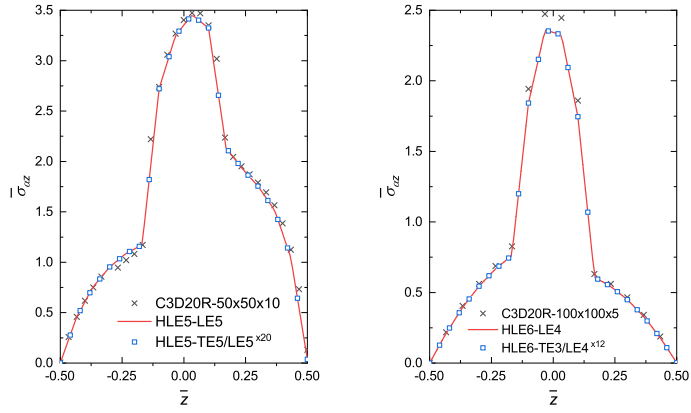


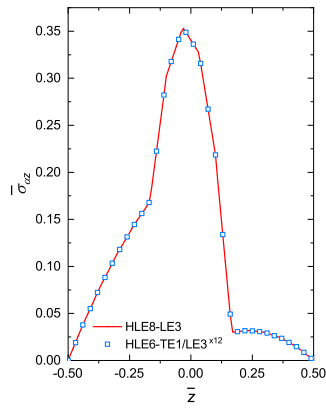
Figure 9: NDK models with variable TE/LE nodal capabilities the three-layered spherical shells under local pressure.

Fig.14 reports comprehensive comparisons of different FE models used in the analysis of the spherical shells subjected to local pressure concerning the



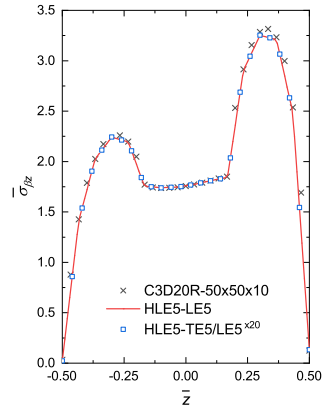
(a) $R/h = 10$

(b) $R/h = 100$

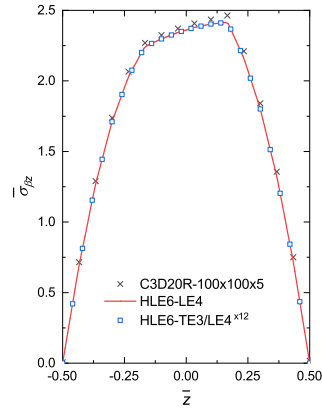


(c) $R/h = 1000$

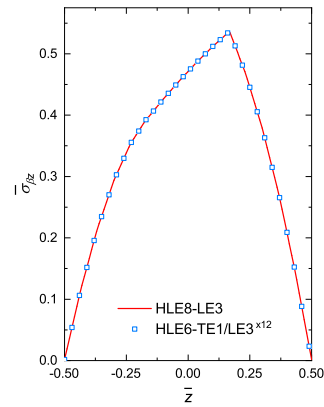
Figure 10: Through-the-thickness variation of $\bar{\sigma}_{\alpha z}$ through $(\frac{a}{25}, 0, \bar{z})$ on the three-layered spherical shells under local pressure.



(a) $R/h = 10$



(b) $R/h = 100$



(c) $R/h = 1000$

Figure 11: Through-the-thickness variation of $\bar{\sigma}_{\beta z}$ through $(0, \frac{2b}{25}, \bar{z})$ on the three-layered spherical shells under local pressure.

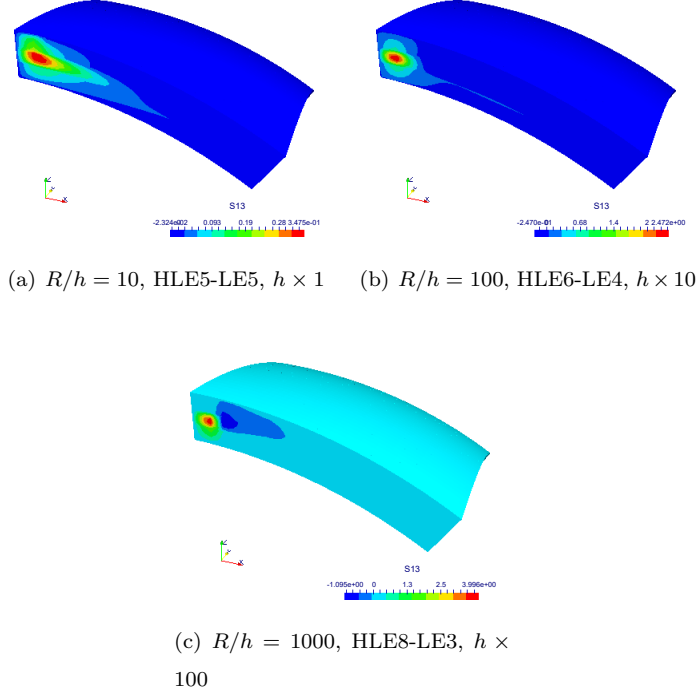


Figure 12: Contour-plots of $\sigma_{\alpha z}$ on the three-layered spherical shells under local pressure, obtained with uniformly refined FE models.

Table 10: A comparison between uniformly refined models and NDK models for the three-layered spherical shells under local pressure regarding computational costs.

R/h	Element	Theory	DOFs	Reduction of DOFs	Relative CPU time \bar{t}	Reduction of CPU time
10	HLE5	LE5	62448	–	88.9	–
		TE5/LE5 $\times 20$	31998	48.8%	41.6	53.2%
100	HLE6	LE4	71019	–	89.2	–
		TE3/LE4 $\times 12$	28521	59.8%	27.0	69.7%
1000	HLE8	LE3	94830	–	142.1	–
		TE1/LE3 $\times 12$	28974	69.4%	24.6	82.7%

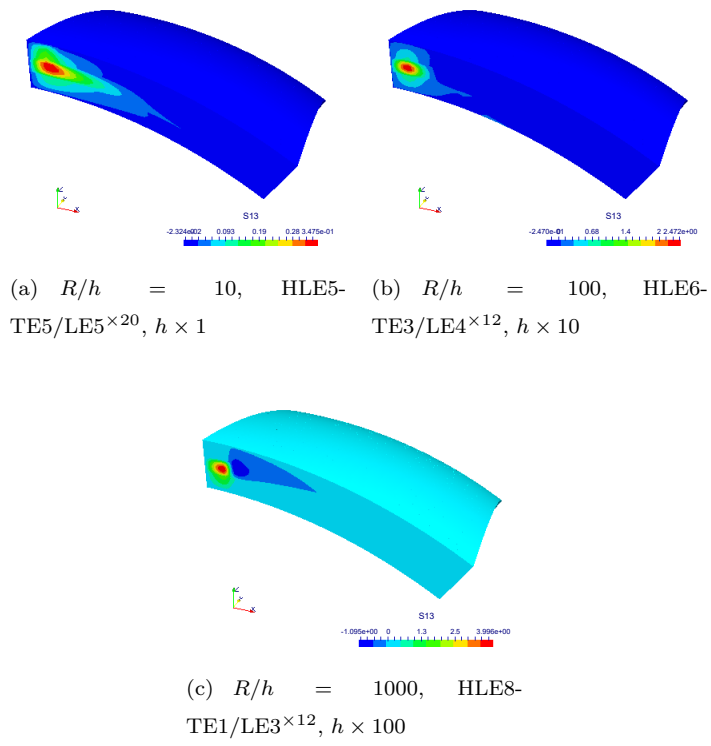
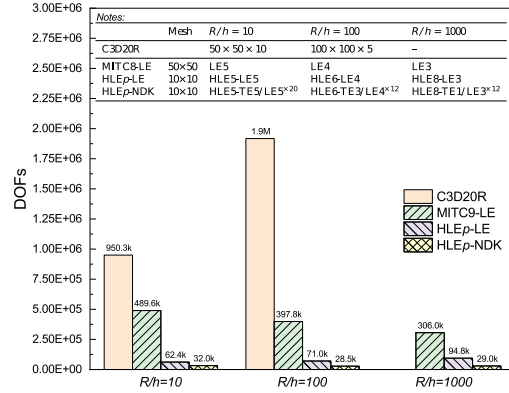


Figure 13: Contour-plots of $\sigma_{\alpha z}$ on the three-layered spherical shells under local pressure, obtained with NDK FE models.

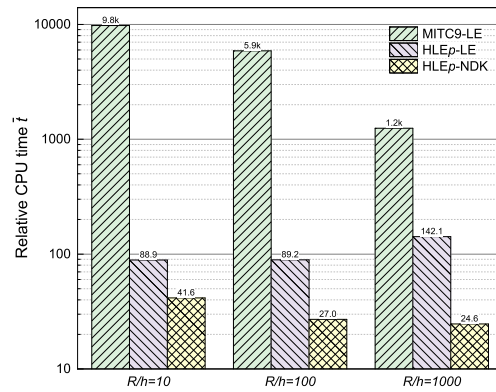
efficiency. The models listed are those who give the best solutions within their
 category as stated in Fig.14(a). Considering the DOFs as shown in Fig.14(a),
 335 the costs of the C3D20R models increase significantly when the shell gets thinner
 from $R/h = 10$ to $R/h = 100$. The refined shell elements are much more efficient
 with comparable accuracy and are less sensitive to the increase of the radius-to-
 thickness ratio. Compared to the locking-free MITC9 elements, the higher-order
 HLE elements are also effective in the mitigation of locking and are even more
 340 economical. HLE element models with NDK are the most efficient, and the
 DOFs used for the moderate-thick ($R/h = 10$) and thin ($R/h = 100$) shells take
 up only 3.4% and 1.5% of DOFs used by C3D20R models, respectively. Fig.14(b)
 compares the CPU time consumptions of different FE models when solving the
 equation systems. The MITC9-LE models show a descending trend regarding
 345 the CPU time consumption with the decrease of the shell thickness. Differently,
 HLE p -LE models with uniform kinematic refinement reveal a slightly increasing
 trend. The efficiency of HLE-NDK models is even more clear concerning the
 time consumption than the DOFs. For the shells with $R/h = 10, 100$ and 1000 ,
 the CPU time consumed in the solution process by HLE p -NDK models takes up
 350 only 0.4%, 0.5%, and 2.0% of that spent by the MITC9-LE models, separately.
 In fact, in engineering simulations, pre-processing, especially meshing takes up
 most the total work time (e.g., 80%). If the re-meshing work can be simplified or
 avoided, the simulations can speed up considerably. The proposed HLE p -NDK
 models can be exploited for this purpose.

355 4. Conclusions

This paper presents an adaptive refinement approach based on Node-Dependent
 Kinematics (NDK) for shell finite element (FE) models. Derived from Carrera
 Unified Formulation (CUF), the proposed models support two levels of mathe-
 matical refinements, namely the kinematic refinement with high-fidelity theories,
 360 and the refinement of the shape function based on the Hierarchical Legendre
 polynomial Expansions (HLE). Moreover, NDK technique allows the kinematic



(a) Total number of degrees of freedom (DOFs)



(b) Relative CPU time consumption \bar{t}

Figure 14: Comparison of various FE models regarding numerical efficiency in the analysis of the three-layered spherical shells under local pressure.

refinement to be related to the shape functions in the critical region which can be adjustably defined. This adaptable refinement FE approach can help to construct FE models for the analysis of laminated shell structures with optimal efficiency conveniently, and reduce the re-meshing work to the minimum. Through the numerical investigations, the following conclusions can be drawn:

- The two levels of mathematical refinement of FE models, namely the refined kinematics assumption over the shell thickness and the increase of the polynomial degree of the p -version element, empowers one to fully utilize the capabilities of given set of 2D mesh grids in obtaining accurate structural responses with 3D accuracy in an efficient way;
- The locking can be alleviated by increasing the polynomial degree of the HLE shell elements to a sufficiently high order;
- By employing Node-Dependent Kinematics (NDK) technique, a local refinement on the chosen nodes can be carried in an adaptable way, and the computational costs can be further reduced without sacrificing the solution accuracy;
- The appropriately chosen local zone with LW models and the adequately refined ESL kinematics for the non-critical region are both crucial for the successful construction of the NDK FE models.

In summary, the NDK technique can be used to construct refined shell FE models with adaptable accuracy, allowing enhanced solutions only in given, critical regions of interest. Also, the proposed method is scalable for a wide range of structural problems, such as failure onset and delamination in layered structures. As future work, automatic adaptive routines can be developed for engineering simulations.

5. Acknowledgement

This research work has been carried out within the project FULLCOMP (FULLy analysis, design, manufacturing, and health monitoring of COMPOSITE

390 structures), funded by the European Union Horizon 2020 Research and Innova-
 tion program under the Marie Skłodowska Curie grant agreement No. 642121.

E. Carrera also acknowledges the Russian Science Foundation under grant
 N 18-19-00092.

Appendix A Stiffness Fundamental Nuclei (FNs) for Node-Dependent Kinematics shell FE formulations

395

$$\begin{aligned}
 K_{\alpha\alpha}^{k,ij\tau s} = & \tilde{C}_{11} \triangleleft N_{i,\alpha} N_{j,\alpha} \triangleright_{\Omega} \triangleleft F_{\tau}^i F_s^j \frac{H_{\beta}}{H_{\alpha}} \triangleright_{A_k} + \tilde{C}_{16} \triangleleft N_{i,\alpha} N_{j,\beta} \triangleright_{\Omega} \triangleleft F_{\tau}^i F_s^j \triangleright_{A_k} \\
 & + \tilde{C}_{55} \triangleleft N_i N_j \triangleright_{\Omega} \triangleleft F_{\tau,z}^i F_{s,z}^j H_{\alpha} H_{\beta} \triangleright_{A_k} - \tilde{C}_{55} \frac{1}{R_{\alpha}} \triangleleft N_i N_j \triangleright_{\Omega} \triangleleft F_{\tau}^i F_s^j H_{\beta} \triangleright_{A_k} \\
 & - \tilde{C}_{55} \frac{1}{R_{\alpha}} \triangleleft N_i N_j \triangleright_{\Omega} \triangleleft F_{\tau,z}^i F_s^j H_{\beta} \triangleright_{A_k} + \tilde{C}_{55} \frac{1}{R_{\alpha}^2} \triangleleft N_i N_j \triangleright_{\Omega} \triangleleft F_{\tau}^i F_s^j \frac{H_{\beta}}{H_{\alpha}} \triangleright_{A_k} \\
 & + \tilde{C}_{16} \triangleleft N_{i,\beta} N_{j,\alpha} \triangleright_{\Omega} \triangleleft F_{\tau}^i F_s^j \triangleright_{A_k} + \tilde{C}_{66} \triangleleft N_{i,\beta} N_{j,\beta} \triangleright_{\Omega} \triangleleft F_{\tau}^i F_s^j \frac{H_{\alpha}}{H_{\beta}} \triangleright_{A_k}
 \end{aligned} \tag{A.1}$$

$$\begin{aligned}
 K_{\alpha\beta}^{k,ij\tau s} = & \tilde{C}_{12} \triangleleft N_{i,\beta} N_{j,\alpha} \triangleright_{\Omega} \triangleleft F_{\tau}^i F_s^j \triangleright_{A_k} + \tilde{C}_{26} \triangleleft N_{i,\beta} N_{j,\beta} \triangleright_{\Omega} \triangleleft F_{\tau}^i F_s^j \frac{H_{\alpha}}{H_{\beta}} \triangleright_{A_k} \\
 & + \tilde{C}_{45} \triangleleft N_j N_i \triangleright_{\Omega} \triangleleft F_{\tau,z}^i F_{s,z}^j H_{\alpha} H_{\beta} \triangleright_{A_k} - \tilde{C}_{45} \frac{1}{R_{\beta}} \triangleleft N_i N_j \triangleright_{\Omega} \triangleleft F_{\tau}^i F_s^j H_{\alpha} \triangleright_{A_k} \\
 & - \tilde{C}_{45} \frac{1}{R_{\alpha}} \triangleleft N_i N_j \triangleright_{\Omega} \triangleleft F_{\tau,z}^i F_s^j H_{\beta} \triangleright_{A_k} + \tilde{C}_{45} \frac{1}{R_{\alpha} R_{\beta}} \triangleleft N_i N_j \triangleright_{\Omega} \triangleleft F_{\tau}^i F_s^j \triangleright_{A_k} \\
 & + \tilde{C}_{16} \triangleleft N_{i,\alpha} N_{j,\alpha} \triangleright_{\Omega} \triangleleft F_{\tau}^i F_s^j \frac{H_{\beta}}{H_{\alpha}} \triangleright_{A_k} + \tilde{C}_{66} \triangleleft N_{i,\alpha} N_{j,\beta} \triangleright_{\Omega} \triangleleft F_{\tau}^i F_s^j \triangleright_{A_k}
 \end{aligned} \tag{A.2}$$

$$\begin{aligned}
 K_{\alpha z}^{k,ij\tau s} = & \tilde{C}_{11} \frac{1}{R_{\alpha}} \triangleleft N_i N_{j,\alpha} \triangleright_{\Omega} \triangleleft F_{\tau}^i F_s^j \frac{H_{\beta}}{H_{\alpha}} \triangleright_{A_k} + \tilde{C}_{16} \frac{1}{R_{\alpha}} \triangleleft N_i N_{j,\beta} \triangleright_{\Omega} \triangleleft F_{\tau}^i F_s^j \triangleright_{A_k} \\
 & + \tilde{C}_{12} \frac{1}{R_{\beta}} \triangleleft N_i N_{j,\alpha} \triangleright_{\Omega} \triangleleft F_{\tau}^i F_s^j \triangleright_{A_k} + \tilde{C}_{26} \frac{1}{R_{\beta}} \triangleleft N_i N_{j,\beta} \triangleright_{\Omega} \triangleleft F_{\tau}^i F_s^j \frac{H_{\alpha}}{H_{\beta}} \triangleright_{A_k} \\
 & + \tilde{C}_{13} \triangleleft N_i N_{j,\alpha} \triangleright_{\Omega} \triangleleft F_{\tau,z}^i F_s^j H_{\beta} \triangleright_{A_k} + \tilde{C}_{36} \triangleleft N_i N_{j,\beta} \triangleright_{\Omega} \triangleleft F_{\tau,z}^i F_s^j H_{\alpha} \triangleright_{A_k} \\
 & + \tilde{C}_{55} \triangleleft N_{i,\alpha} N_j \triangleright_{\Omega} \triangleleft F_{\tau}^i F_s^j H_{\beta} \triangleright_{A_k} - \tilde{C}_{55} \frac{1}{R_{\alpha}} \triangleleft N_{i,\alpha} N_j \triangleright_{\Omega} \triangleleft F_{\tau}^i F_s^j \frac{H_{\beta}}{H_{\alpha}} \triangleright_{A_k} \\
 & + \tilde{C}_{45} \triangleleft N_{i,\beta} N_j \triangleright_{\Omega} \triangleleft F_{\tau}^i F_s^j H_{\alpha} \triangleright_{A_k} - \tilde{C}_{45} \frac{1}{R_{\alpha}} \triangleleft N_{i,\beta} N_j \triangleright_{\Omega} \triangleleft F_{\tau}^i F_s^j \triangleright_{A_k}
 \end{aligned} \tag{A.3}$$

$$\begin{aligned}
K_{\beta\alpha}^{k,ij\tau s} &= \tilde{C}_{12} \triangleleft N_{i,\alpha} N_{j,\beta} \triangleright_{\Omega} \triangleleft F_{\tau}^i F_s^j \triangleright_{A_k} + \tilde{C}_{16} \triangleleft N_{i,\alpha} N_{j,\alpha} \triangleright_{\Omega} \triangleleft F_{\tau}^i F_s^j \frac{H_{\beta}}{H_{\alpha}} \triangleright_{A_k} \\
&+ \tilde{C}_{45} \triangleleft N_i N_j \triangleright_{\Omega} \triangleleft F_{\tau,z}^i F_{s,z}^j H_{\alpha} H_{\beta} \triangleright_{A_k} - \tilde{C}_{45} \frac{1}{R_{\alpha}} \triangleleft N_i N_j \triangleright_{\Omega} \triangleleft F_{\tau}^i F_s^j H_{\beta} \triangleright_{A_k} \\
&- \tilde{C}_{45} \frac{1}{R_{\beta}} \triangleleft N_i N_j \triangleright_{\Omega} \triangleleft F_{\tau,z}^i F_s^j H_{\alpha} \triangleright_{A_k} + \tilde{C}_{45} \frac{1}{R_{\alpha} R_{\beta}} \triangleleft N_i N_j \triangleright_{\Omega} \triangleleft F_{\tau}^i F_s^j \triangleright_{A_k} \\
&+ \tilde{C}_{26} \triangleleft N_{i,\beta} N_{j,\beta} \triangleright_{\Omega} \triangleleft F_{\tau}^i F_s^j \frac{H_{\alpha}}{H_{\beta}} \triangleright_{A_k} + \tilde{C}_{66} \triangleleft N_{i,\beta} N_{j,\alpha} \triangleright_{\Omega} \triangleleft F_{\tau}^i F_s^j \triangleright_{A_k}
\end{aligned} \tag{A.4}$$

$$\begin{aligned}
K_{\beta\beta}^{k,ij\tau s} &= \tilde{C}_{22} \triangleleft N_{i,\beta} N_{j,\beta} \triangleright_{\Omega} \triangleleft F_{\tau}^i F_s^j \frac{H_{\alpha}}{H_{\beta}} \triangleright_{A_k} + \tilde{C}_{26} \triangleleft N_{i,\beta} N_{j,\alpha} \triangleright_{\Omega} \triangleleft F_{\tau}^i F_s^j \triangleright_{A_k} \\
&+ \tilde{C}_{44} \triangleleft N_i N_j \triangleright_{\Omega} \triangleleft F_{\tau,z}^i F_{s,z}^j H_{\alpha} H_{\beta} \triangleright_{A_k} - \tilde{C}_{44} \frac{1}{R_{\beta}} \triangleleft N_i N_j \triangleright_{\Omega} \triangleleft F_{\tau}^i F_{s,z}^j H_{\alpha} \triangleright_{A_k} \\
&- \tilde{C}_{44} \frac{1}{R_{\beta}} \triangleleft N_i N_j \triangleright_{\Omega} \triangleleft F_{\tau,z}^i F_s^j H_{\alpha} \triangleright_{A_k} + \tilde{C}_{44} \frac{1}{R_{\beta}^2} \triangleleft N_i N_j \triangleright_{\Omega} \triangleleft F_{\tau}^i F_s^j \frac{H_{\alpha}}{H_{\beta}} \triangleright_{A_k} \\
&+ \tilde{C}_{26} \triangleleft N_{i,\alpha} N_{j,\beta} \triangleright_{\Omega} \triangleleft F_{\tau}^i F_s^j \triangleright_{A_k} + \tilde{C}_{66} \triangleleft N_{i,\alpha} N_{j,\alpha} \triangleright_{\Omega} \triangleleft F_{\tau}^i F_s^j \frac{H_{\beta}}{H_{\alpha}} \triangleright_{A_k}
\end{aligned} \tag{A.5}$$

$$\begin{aligned}
K_{\beta z}^{k,ij\tau s} &= \tilde{C}_{12} \frac{1}{R_{\alpha}} \triangleleft N_i N_{j,\beta} \triangleright_{\Omega} \triangleleft F_{\tau}^i F_s^j \triangleright_{A_k} + \tilde{C}_{16} \frac{1}{R_{\alpha}} \triangleleft N_i N_{j,\alpha} \triangleright_{\Omega} \triangleleft F_{\tau}^i F_s^j \frac{H_{\beta}}{H_{\alpha}} \triangleright_{A_k} \\
&+ \tilde{C}_{22} \frac{1}{R_{\beta}} \triangleleft N_i N_{j,\beta} \triangleright_{\Omega} \triangleleft F_{\tau}^i F_s^j \frac{H_{\alpha}}{H_{\beta}} \triangleright_{A_k} + \tilde{C}_{26} \frac{1}{R_{\beta}} \triangleleft N_i N_{j,\alpha} \triangleright_{\Omega} \triangleleft F_{\tau}^i F_s^j \triangleright_{A_k} \\
&+ \tilde{C}_{23} \triangleleft N_i N_{j,\beta} \triangleright_{\Omega} \triangleleft F_{\tau,z}^i F_s^j H_{\alpha} \triangleright_{A_k} + \tilde{C}_{36} \triangleleft N_i N_{j,\alpha} \triangleright_{\Omega} \triangleleft F_{\tau,z}^i F_s^j H_{\beta} \triangleright_{A_k} \\
&+ \tilde{C}_{45} \triangleleft N_{i,\alpha} N_j \triangleright_{\Omega} \triangleleft F_{\tau}^i F_{s,z}^j H_{\beta} \triangleright_{A_k} - \tilde{C}_{45} \frac{1}{R_{\beta}} \triangleleft N_{i,\alpha} N_j \triangleright_{\Omega} \triangleleft F_{\tau}^i F_s \triangleright_{A_k} \\
&+ \tilde{C}_{44} \triangleleft N_{i,\beta} N_j \triangleright_{\Omega} \triangleleft F_{\tau}^i F_{s,z}^j H_{\alpha} \triangleright_{A_k} - \tilde{C}_{44} \frac{1}{R_{\beta}} \triangleleft N_{i,\beta} N_j \triangleright_{\Omega} \triangleleft F_{\tau}^i F_s \frac{H_{\alpha}}{H_{\beta}} \triangleright_{A_k}
\end{aligned} \tag{A.6}$$

$$\begin{aligned}
K_{z\alpha}^{k,ij\tau s} &= \tilde{C}_{11} \frac{1}{R_\alpha} \langle N_{i,\alpha} N_j \rangle_\Omega \langle F_\tau^i F_s^j \frac{H_\beta}{H_\alpha} \rangle_{A_k} \triangleright_{A_k} + \tilde{C}_{12} \frac{1}{R_\beta} \langle N_{i,\alpha} N_j \rangle_\Omega \langle F_\tau^i F_s^j \rangle_{A_k} \\
&+ \tilde{C}_{13} \langle N_{i,\alpha} N_j \rangle_\Omega \langle F_\tau^i F_{s,z}^j H_\beta \rangle_{A_k} + \tilde{C}_{55} \langle N_i N_{j,\alpha} \rangle_\Omega \langle F_{\tau,z}^i F_s^j H_\beta \rangle_{A_k} \\
&- \tilde{C}_{55} \frac{1}{R_\alpha} \langle N_i N_{j,\alpha} \rangle_\Omega \langle F_\tau^i F_s^j \frac{H_\beta}{H_\alpha} \rangle_{A_k} + \tilde{C}_{45} \langle N_i N_{j,\beta} \rangle_\Omega \langle F_{\tau,z}^i F_s^j H_\alpha \rangle_{A_k} \\
&- \tilde{C}_{45} \frac{1}{R_\alpha} \langle N_i N_{j,\beta} \rangle_\Omega \langle F_\tau^i F_s^j \rangle_{A_k} + \tilde{C}_{16} \frac{1}{R_\alpha} \langle N_{i,\beta} N_j \rangle_\Omega \langle F_\tau^i F_s^j \rangle_{A_k} \\
&+ \tilde{C}_{26} \frac{1}{R_\beta} \langle N_{i,\beta} N_j \rangle_\Omega \langle F_\tau^i F_s^j \frac{H_\alpha}{H_\beta} \rangle_{A_k} + \tilde{C}_{36} \langle N_{i,\beta} N_j \rangle_\Omega \langle F_\tau^i F_{s,z}^j H_\alpha \rangle_{A_k}
\end{aligned} \tag{A.7}$$

$$\begin{aligned}
K_{z\beta}^{k,ij\tau s} &= \tilde{C}_{12} \frac{1}{R_\alpha} \langle N_{i,\beta} N_j \rangle_\Omega \langle F_\tau^i F_s^j \rangle_{A_k} + \tilde{C}_{22} \frac{1}{R_\beta} \langle N_j N_{i,\beta} \rangle_\Omega \langle F_\tau^i F_s^j \frac{H_\alpha}{H_\beta} \rangle_{A_k} \\
&+ \tilde{C}_{23} \langle N_{i,\beta} N_j \rangle_\Omega \langle F_\tau^i F_{s,z}^j H_\alpha \rangle_{A_k} + \tilde{C}_{45} \langle N_i N_{j,\alpha} \rangle_\Omega \langle F_{\tau,z}^i F_s^j H_\beta \rangle_{A_k} \\
&- \tilde{C}_{45} \frac{1}{R_\beta} \langle N_i N_{j,\alpha} \rangle_\Omega \langle F_\tau^i F_s^j \rangle_{A_k} + \tilde{C}_{44} \langle N_i N_{j,\beta} \rangle_\Omega \langle F_{\tau,z}^i F_s^j H_\alpha \rangle_{A_k} \\
&- \tilde{C}_{44} \frac{1}{R_\beta} \langle N_i N_{j,\beta} \rangle_\Omega \langle F_\tau^i F_s^j \frac{H_\alpha}{H_\beta} \rangle_{A_k} + \tilde{C}_{16} \frac{1}{R_\alpha} \langle N_{i,\alpha} N_j \rangle_\Omega \langle F_\tau^i F_s^j \frac{H_\beta}{H_\alpha} \rangle_{A_k} \\
&+ \tilde{C}_{26} \frac{1}{R_\beta} \langle N_{i,\alpha} N_j \rangle_\Omega \langle F_\tau^i F_s^j \rangle_{A_k} + \tilde{C}_{36} \langle N_{i,\alpha} N_j \rangle_\Omega \langle F_\tau^i F_{s,z}^j H_\beta \rangle_{A_k}
\end{aligned} \tag{A.8}$$

$$\begin{aligned}
K_{zz}^{k,ij\tau s} &= \tilde{C}_{11} \frac{1}{R_\alpha^2} \langle N_i N_j \rangle_\Omega \langle F_\tau^i F_s^j \frac{H_\beta}{H_\alpha} \rangle_{A_k} + 2\tilde{C}_{12} \frac{1}{R_\alpha R_\beta} \langle N_i N_j \rangle_\Omega \langle F_\tau^i F_s^j \rangle_{A_k} \\
&+ \tilde{C}_{13} \frac{1}{R_\alpha} \langle N_i N_j \rangle_\Omega \langle F_\tau^i F_{s,z}^j H_\beta \rangle_{A_k} + \tilde{C}_{22} \frac{1}{R_\beta^2} \langle N_i N_j \rangle_\Omega \langle F_\tau^i F_s^j \frac{H_\alpha}{H_\beta} \rangle_{A_k} \\
&+ \tilde{C}_{23} \frac{1}{R_\beta} \langle N_i N_j \rangle_\Omega \langle F_\tau^i F_{s,z}^j H_\alpha \rangle_{A_k} + \tilde{C}_{13} \frac{1}{R_\alpha} \langle N_i N_j \rangle_\Omega \langle F_{\tau,z}^i F_s^j H_\beta \rangle_{A_k} \\
&+ \tilde{C}_{23} \frac{1}{R_\beta} \langle N_i N_j \rangle_\Omega \langle F_{\tau,z}^i F_s^j H_\alpha \rangle_{A_k} + \tilde{C}_{33} \langle N_i N_j \rangle_\Omega \langle F_{\tau,z}^i F_{s,z}^j H_\alpha H_\beta \rangle_{A_k} \\
&+ \tilde{C}_{55} \langle N_{i,\alpha} N_{j,\alpha} \rangle_\Omega \langle F_\tau^i F_s^j \frac{H_\beta}{H_\alpha} \rangle_{A_k} + \tilde{C}_{45} \langle N_{i,\alpha} N_{j,\beta} \rangle_\Omega \langle F_\tau^i F_s^j \rangle_{A_k} \\
&+ \tilde{C}_{45} \langle N_{i,\beta} N_{j,\alpha} \rangle_\Omega \langle F_\tau^i F_s^j \rangle_{A_k} + \tilde{C}_{44} \langle N_{i,\beta} N_{j,\beta} \rangle_\Omega \langle F_\tau^i F_s^j \frac{H_\alpha}{H_\beta} \rangle_{A_k}
\end{aligned} \tag{A.9}$$

where $\langle \cdots \rangle_\Omega$ indicates $\int_\Omega \cdots d\alpha d\beta$, and $\langle \cdots \rangle_{A_k}$ represents $\int_{A_k} \cdots dz_k$. Ω stands for the middle-surface in-plane domain of the shell element, and A_k

the thickness domain of layer k .

Appendix B List of acronyms

The following acronyms have been introduced in the text:

FE(s)	Finite element(s)
CUF	Carrera Unified Formulation
LW	Layer-Wise
ESL	Equivalent Single-Layer
HLE	Hierarchical Legendre polynomial Expansions
NDK	Node-Dependent Kinematics
FSDT	First-Order Shear Deformation Theory
FNs	Fundamental Nuclei
TE	Taylor Expansions
LE	Lagrange Expansions
1D	One-dimensional
2D	Two-dimensional
3D	Three-dimensional
Q4	4-node quadrilateral Lagrangian element
Q9	9-node quadrilateral Lagrangian element
MITC	Mixed Interpolation of Tensorial Components
MITC9	Q9 with Mixed Interpolation of Tensorial Components
C3D20R	20-node quadratic brick element with reduced integration
DOFs	Degrees of freedom

References

- [1] W. Koiter, On the foundations of the linear theory of thin elastic shell, Proc Kon Nederl Akad Wetensch 73 (3) (1970) 169–195.
- [2] P. Naghdi, The theory of plates and shells, Handbuch der Physik, vol. VI
405 a-2 (1972) 425–640.
- [3] J. N. Reddy, A simple higher-order theory for laminated composite plates, Journal of Applied Mechanics 51 (4) (1984) 745–752.
- [4] J. N. Reddy, Mechanics of laminated composite plates and shells: theory and analysis, CRC Press, 2004.
- 410 [5] A. N. Palazotto, Nonlinear analysis of shell structures, AIAA Series, 1992.
- [6] E. Carrera, Theories and finite elements for multilayered, anisotropic, composite plates and shells, Archives of Computational Methods in Engineering 9 (2) (2002) 87–140.
- [7] E. Carrera, M. Cinefra, M. Petrolo, E. Zappino, Finite element analysis of
415 structures through Unified Formulation, John Wiley & Sons, 2014.
- [8] M. Cinefra, E. Carrera, Shell finite elements with different through-the-thickness kinematics for the linear analysis of cylindrical multilayered structures, International Journal for Numerical Methods in Engineering 93 (2) (2013) 160–182.
- 420 [9] M. Cinefra, S. Valvano, A variable kinematic doubly-curved MITC9 shell element for the analysis of laminated composites, Mechanics of Advanced Materials and Structures 23 (11) (2016) 1312–1325.
- [10] E. Carrera, M. Cinefra, G. Li, G. Kulikov, MITC9 shell finite elements with
425 miscellaneous through-the-thickness functions for the analysis of laminated structures, Composite Structures 154 (2016) 360–373.

- [11] E. Carrera, M. Cinefra, G. Li, Refined finite element solutions for anisotropic laminated plates, *Composite Structures* 183 (2018) 63–76.
- [12] M. Petrolo, A. Lamberti, F. Miglioretti, Best theory diagram for metallic and laminated composite plates, *Mechanics of Advanced Materials and Structures* 23 (9) (2016) 1114–1130.
- 430
- [13] M. Cinefra, E. Carrera, A. Lamberti, M. Petrolo, Best theory diagrams for multilayered plates considering multifield analysis, *Journal of Intelligent Material Systems and Structures* 28 (16) (2017) 2184–2205.
- [14] J. Yarasca, J. Mantari, M. Petrolo, E. Carrera, Multiobjective best theory diagrams for cross-ply composite plates employing polynomial, zig-zag, trigonometric and exponential thickness expansions, *Composite Structures* 176 (2017) 860–876.
- 435
- [15] M. Cinefra, M. Petrolo, G. Li, E. Carrera, Hygrothermal analysis of multilayered composite plates by variable kinematic finite elements, *Journal of Thermal Stresses* 40 (12) (2017) 1502–1522.
- 440
- [16] M. Cinefra, M. Petrolo, G. Li, E. Carrera, Variable kinematic shell elements for composite laminates accounting for hygrothermal effects, *Journal of Thermal Stresses* 40 (12) (2017) 1523–1544.
- [17] E. Carrera, S. Valvano, Analysis of laminated composite structures with embedded piezoelectric sheets by variable kinematic shell elements, *Journal of Intelligent Material Systems and Structures* 28 (20) (2017) 2959–2987.
- 445
- [18] E. Carrera, E. Zappino, One-dimensional finite element formulation with node-dependent kinematics, *Computers & Structures* 192 (2017) 114–125.
- [19] E. Carrera, A. Pagani, S. Valvano, Multilayered plate elements accounting for refined theories and node-dependent kinematics, *Composites Part B: Engineering* 114 (2017) 189–210.
- 450

- [20] E. Carrera, E. Zappino, G. Li, Finite element models with node-dependent kinematics for the analysis of composite beam structures, *Composites Part B: Engineering* 132 (Supplement C) (2018) 35 – 48.
- 455 [21] S. Valvano, E. Carrera, Multilayered plate elements with node-dependent kinematics for the analysis of composite and sandwich structures, *Facta Universitatis, Series: Mechanical Engineering* 15 (1) (2017) 1–30.
- [22] E. Zappino, G. Li, A. Pagani, E. Carrera, Global-local analysis of laminated plates by node-dependent kinematic finite elements with variable ESL/LW capabilities, *Composite Structures* 172 (2017) 1–14.
- 460 [23] M. Cinefra, S. Valvano, E. Carrera, A layer-wise MITC9 finite element for the free-vibration analysis of plates with piezo-patches, *International Journal of Smart and Nano Materials* 6 (2) (2015) 85–104.
- [24] E. Carrera, E. Zappino, G. Li, Analysis of beams with piezo-patches by node-dependent kinematic finite element method models, *Journal of Intelligent Material Systems and Structures* 29 (7) (2018) 1379–1393.
- 465 [25] E. Carrera, S. Valvano, G. Kulikov, Multilayered plate elements with node-dependent kinematics for electro-mechanical problems, *International Journal of Smart and Nano Materials* (2017) 1–39.
- 470 [26] A. Peano, Hierarchies of conforming finite elements for plane elasticity and plate bending, *Computers & Mathematics with Applications* 2 (3-4) (1976) 211–224.
- [27] B. Szabó, A. Mehta, p-convergent finite element approximations in fracture mechanics, *International Journal for Numerical Methods in Engineering* 12 (3) (1978) 551–560.
- 475 [28] O. C. Zienkiewicz, J. D. S. Gago, D. W. Kelly, The hierarchical concept in finite element analysis, *Computers & Structures* 16 (1) (1983) 53–65.
- [29] B. A. Szabó, I. Babuška, *Finite element analysis*, John Wiley & Sons, 1991.

- [30] B. Szabó, A. Düster, E. Rank, The p-Version of the Finite Element Method, Wiley Online Library, 2004.
- [31] E. Carrera, A. de Miguel, A. Pagani, Hierarchical theories of structures based on Legendre polynomial expansions with finite element applications, International Journal of Mechanical Sciences 120 (2017) 286–300.
- [32] A. Pagani, A. de Miguel, M. Petrolo, E. Carrera, Analysis of laminated beams via Unified Formulation and Legendre polynomial expansions, Composite Structures 156 (2016) 78 – 92, 70th Anniversary of Professor J. N. Reddy.
- [33] E. Zappino, G. Li, A. Pagani, E. Carrera, A. de Miguel, Use of higher-order legendre polynomials for multilayered plate elements with node-dependent kinematics, Composite Structures.
- [34] B. A. Szabó, Mesh design for the p-version of the finite element method, Computer Methods in Applied Mechanics and Engineering 55 (1-2) (1986) 181–197.
- [35] M. Suri, Analytical and computational assessment of locking in the hp finite element method, Computer Methods in Applied Mechanics and Engineering 133 (3-4) (1996) 347–371.
- [36] A. Düster, H. Bröker, E. Rank, The p-version of the finite element method for three-dimensional curved thin walled structures, International Journal for Numerical Methods in Engineering 52 (7) (2001) 673–703.
- [37] M. Ainsworth, p-and hp-Finite Element Methods. Theory and Applications in Solid and Fluid Mechanics, Mathematics of Computation 70 (235) (2001) 1335–1337.
- [38] E. N. Dvorkin, K.-J. Bathe, A continuum mechanics based four-node shell element for general non-linear analysis, Engineering Computations 1 (1) (1984) 77–88.

- [39] M. L. Bucelem, K.-J. Bathe, Higher-order mitc general shell elements, *International Journal for Numerical Methods in Engineering* 36 (21) (1993) 3729–3754.
- [40] A. W. Leissa, *Vibration of shells*, Vol. 288, Scientific and Technical Information Office, National Aeronautics and Space Administration Washington, 1973.
- [41] R. M. Jones, *Buckling of bars, plates, and shells*, Bull Ridge Corporation, 2006.
- [42] T. Varadan, K. Bhaskar, Bending of laminated orthotropic cylindrical shell-san elasticity approach, *Composite Structures* 17 (2) (1991) 141–156.
- [43] J. Reddy, Exact solutions of moderately thick laminated shells, *Journal of Engineering Mechanics* 110 (5) (1984) 794–809.
- [44] C. A. Felippa, *Introduction to finite element methods*, Course Notes, Department of Aerospace Engineeing Sciences, University of Colorado at Boulder, available at [http://www. colorado. edu/engineering/Aerospace/CAS/courses. d/IFEM. d](http://www.colorado.edu/engineering/Aerospace/CAS/courses.d/IFEM.d).
- [45] G. Li, E. Carrera, M. Cinefra, A.G. de Miguel, G. Kulikov, A. Pagani, and E. Zappino, Evaluation of locking in refined hierarchical shell finite elements for laminated structures, *Advanced Modeling and Simulation in Engineering Sciences*. Accepted manuscript.